ANALYSIS OF CATION-TREATED CLAY MICROSTRUCTURE USING ZETA POTENTIAL AND X-RAY DIFFRACTION

By

Rui Guo, B.S., M.S.

A Project Submitted in Partial Fulfillment of the Requirements

for the Degree of

Master of Science

in

Geological Engineering

University of Alaska Fairbanks

December 2018

APPROVED:

Margaret M. Darrow, Committee Chair
Paul A. Metz, Committee Member
Thomas P. Trainor, Committee Member
Margaret M. Darrow, Chair
Department of Mining and Geological Engineering

ABSTRACT

Unfrozen water within cation-treated, fine-grained frozen soils is a key element in cold regions engineering, and is heavily influenced by the surface charge of the soil's clay component. This study investigated the effects of the surface charge of cation-treated clay soils by measuring the zeta potential as a function of temperature, and measuring changes in the micro-structure of frozen cation-treated clays using the x-ray diffraction (XRD) method. I tested five treatments (untreated, and Ca^{2+}, Mg^{2+}, Na^{+}, and K^{+} treatments) of six soils (montmorillonite, kaolinite, illite, illite-smectite, chlorite, and Copper River soil).

The zeta potential demonstrated a negative relationship with temperature change for both above-freezing and sub-freezing conditions (-1 to 20 °C). Temperature had a greater effect on the monovalent-treated soils that contain smectite minerals, which included montmorillonite, illite-smectite, and the Copper River soil. Monovalent cation-treated soils demonstrated large negative trends and more negative zeta potential, whereas divalent cation-treated soils demonstrated less negative trends that were less dependent on temperature. The cation treatment will affect the Debye-length, also affecting the zeta potential and arrangement of clay particles. More negative zeta potential (i.e., soil dominated by monovalent cations) will lead to a dispersed structure, whereas less negative zeta potential (i.e., soil dominated by divalent cations) will lead to a flocculated structure.

XRD research indicated that the montmorillonite samples demonstrated decreased d-spacing compared with the International Center for Diffraction Data (ICDD) standard. The K^{+}-treated montmorillonite, untreated montmorillonite, and untreated illite-smectite samples demonstrated donut-shaped pole figure results, which may indicate that the results are an artifact of sample preparation rather than a reflection of the cation effects on the structure of the clay.

Improved could be made in sample preparation to eliminate ice lens formation during freezing, which may improve the success with the XRD method. Scanning electron microscopy (SEM) should be used to observe the frozen clays, especially montmorillonite, illite-smectite, and the Copper River soil, as it may reveal the internal geometry of voids and the possible relationship between ice and the clay structure, increasing our understanding of the clay structure at the microaggregate scale.

TABLE OF CONTENTS

Page

LIST OF FIGURES

Page

LIST OF TABLES

Page

ACKNOWLEDGEMENTS

I would like to take this opportunity to thank my advisor, Dr. Margaret M. Darrow, for being a constant source of advice and support without which the completion of this thesis would not have been possible. I also thank Dr. Paul A. Metz and Dr. Thomas P. Trainor for being my thesis committee members and for their help and guidance.

This research was supported by the National Science Foundation under Grant No. 1147806.

1. INTRODUCTION AND SCOPE OF WORK

This research focuses on how the surface charge of cation-treated soils may affect the mobility of unfrozen water. The objectives of this research are: 1) to measure the zeta potential of cation-treated clays as a function of temperature; and 2) to measure changes in the micro-structure of the frozen cation-treated clays using the x-ray diffraction (XRD) texture method.

Understanding unfrozen water mobility is of key importance in the strength of frozen soil and in the frost heave process. When the temperature drops below the freezing point, a thin layer of unfrozen water still remains around soil particles. The presence of unfrozen water in frozen soil was first quantified by Bouyoucos (1917) using a dilatometer. Later Nersesova and Tsytovich (1963) indicated that the mass fraction of unfrozen water is highly dependent on a soil's physicochemical attributes, including exchangeable cations and the mineralogical composition of the soil. The quantity and composition of ice and unfrozen water in the frozen soil are not fixed, but in a dynamic equilibrium with the subfreezing temperature. The movement of unfrozen water affects the mass balance of frozen soil systems, frozen soil strength, and frost heave magnitude, and is relevant to geotechnical engineering and agriculture in cold regions with prevelant seasonal frost or permafrost.

In a soil, water can exist: 1) in the soil pore spaces as free water, the movement of which is dominated by the gravitational force; 2) as capillary water (if the diameter of the pore space is submillimeter, this can generate a capillary force that is greater than the gravitational force); or 3) as surface water adsorbed on the clay particles when electrostatic or electrophoresis forces are dominant at a nanometer scale (Henniker 1949). The interaction of water and the cations dissolved in the water with negatively-charged surfaces of clay minerals controls the movement of water at the nanometer scale, while gravity and capillary forces are negligible.

The common exchangeable cations found in soils are Ca^{2+}, Mg^{2+}, Na^{+}, and K^{+}, which are generally referred to as the base cations. These cations can strongly influence the structural conditions of soils with similar mineralogy (Rengasamy and Sumner 1998). If salt solutions are mixed with clay minerals in the lab (called a cation treatment), then the corresponding cation effects found in nature can be analyzed. The electrostatic forces are changed when these cations are exchanged on clay surfaces, which may affect unfrozen water mobility. Zeta potential, which is defined as the average potential at the shear surface (Hunter 1981), is measured to analyze these forces near the surface of the clay particle. As part of this study, I tested the effects of temperature – including subfreezing temperature – and cation treatments on the zeta potential of clay soils, to improve our understanding of temperature effects on unfrozen water mobility.

Clays are phyllosilicate minerals that typically have a particle size of 2-μm equivalent spherical diameter or less (Guggenheim and Martin 1995). Their repeated lattice crystalline structure can trigger constructive interference of x-rays. X-ray diffraction (XRD) is a widely-used technique to determine the mineral composition of a soil sample, since the scattering pattern can be measured and then analyzed to deduce the locations of the atoms in the crystalline structure (Girolami 2015). XRD also can be used to quantify the orientation of clay minerals. Different orientations of clay minerals will change the intensity of reflected x-ray peaks, which are recorded using pole figures. As the second part of this study, I used the XRD texture scan to measure the orientation of individual particles in frozen cation-treated clays. This was to determine if the cation treatments and the freezing process changed the micro-structure of the soil, to understand better how unfrozen water moves through frozen soil.

This thesis consists of six chapters. Chapter 1 is a brief introduction of the topic and a presentation of the scope of this research. Chapter 2 is a literature review that covers clay mineralogy, zeta potential, and the XRD method. In Chapter 3, I detail the preparation of the soil samples, and describe the equipment and methods used for zeta potential tests and XRD measurements. Chapter 4 contains 1) the results of the zeta potential measurements at different temperatures and pH values for the different cation-treated samples, and 2) the results of the XRD powder measurements and pole figure measurements for the sample tested. In Chapter 5, I present possible mechanisms that may explain the experimental results, and discuss the significance of the results with respect to unfrozen water mobility. Finally, Chapter 6 is a summary of my conclusions and suggestions for future research.

2. LITERATURE REVIEW

To understand the electrostatic and electrokinetic processes at the mineral-fluid interface, first we need to understand the structure and properties of clay minerals. Clay minerals are classified as phyllosilicates, or sheet silicates. Clays are the results of dissolution and recrystallization during weathering at the rock-atmosphere interface or water-sediment interface found at the earth's surface.

2.1 Clay mineralogy

Clays are classified as phyllosilicates because their crystallographic structures are thin, sheet-like networks, with a thickness to width or length ratio often near 20 (Velde 1995). These interlinked polyhedral sheets are composed of oxygen anions and silicon, or frequently aluminum, cations. Two elementary polyhedral structures that make up clays are tetrahedral and octahedral (Figure 2.1), linked by highly covalent ionic bonding. The tetrahedra are composed of four oxygen atoms surrounding a silicon atom, and octahedra have six oxygen atoms surrounding a ferrous iron or aluminum ion. The anions are not exclusively oxygen atoms, but also can be hydroxyl groups (Velde 1995).

The crystalline structures of clay minerals can be classified into two big categories based on structural arrangement (Sposito et al. 1999): 1:1 structures, with one tetrahedral layer and one octahedral layer, such as kaolinite; and 2:1 structures that consist of two tetrahedral layers and one octahedral layer, such as illite and montmorillonite. The space between the repeated one tetrahedral layer and one octahedral layer combination (for 1:1 clays), or between the repeated two tetrahedral layers and one octahedral layer combination (for 2:1 clays) is called the

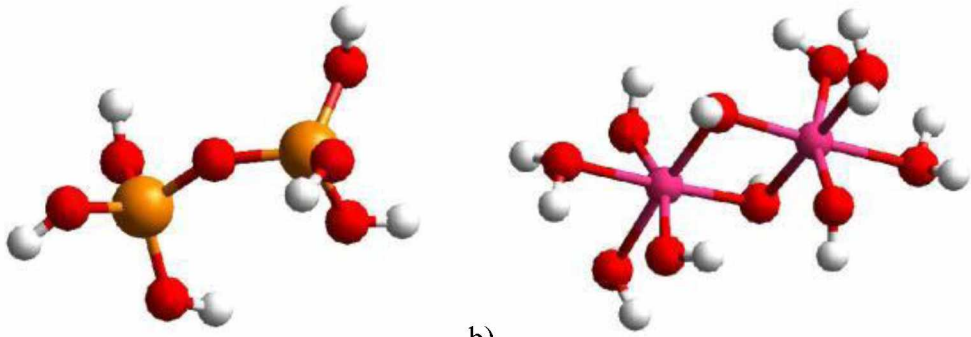

a) b)

Figure 2.1. Polyhedral structures present in clay minerals: a) tetrahedra; and b) octahedra. Red, white, yellow, and pink balls represent oxygen, hydrogen, silicon, and aluminum or iron, respectively. Images are not to scale (taken from Teppen 2000).

interlayer. Another category is 2:1:1, which is similar to a traditional 2:1 structure, but with an additional octahedral layer connecting the repeating 2:1 structures. Chlorite is an example of a 2:1:1 clay. If layers of different kinds of clays alternate with each other, they are called mixed-layer clays, such as illite-smectite. The five common clay minerals that were chosen for this study are montmorillonite, kaolinite, illite, illite-smectite, and chlorite.

Some clay minerals experience isomorphic substitution. If two Al^{3+} cations are substituted for three Mg^{2+} cations (Figure 2.2), then the net charge will not be changed. If substitution of the same number of cations but with different charges happens, however, a structural charge is created that can attract cations and polar molecules (Velde 1995). Because changing pH values and ion-exchange reactions have no influence on this structural charge, it is called the permanent charge, structural charge, or permanent structural charge (Funck 2008).

Surface charge is the electrical potential gradient between the inner and outer surfaces of the dispersed phase in a colloid (Butt et al. 2006). Surface charge is developed by losing or gaining protons (H^+) depending on the pH, and by specific anion/cation adsorption (Bolan et al. 1999). Barrow (1986) used variable charge to describe the surface charge components depending mainly on the pH of the soil solution. The balance of negative-surface-charge sites and the forces of attraction/repulsion arising from hydration of the interlayer cations also controls the crystalline swelling (Laird 1996, 2006).

The net total particle charge is the sum of the permanent charge and variable surface charge. Electrical potentials formed by the net particle charge can influence electrophoretic mobility (Schulthess and Sparks 1988), and flocculation/dispersion (Suarez et al. 1984). In nature, permanent charges are usually compensated by the cation occupation in the clay

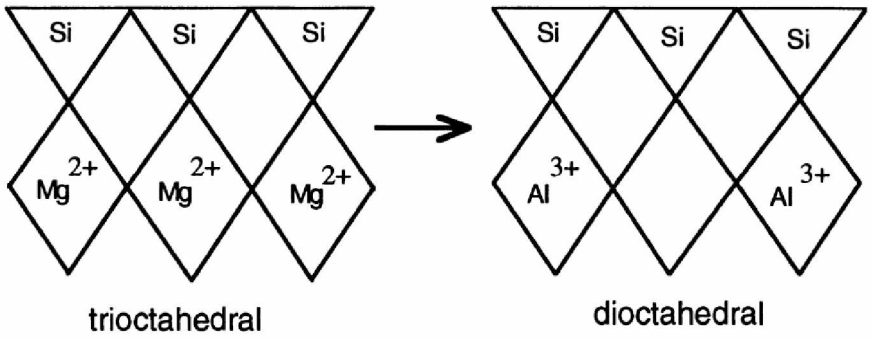

Figure 2.2. The dioctahedral-trioctahedral substitution with the same charge, side view (taken from Velde 1995).

interlayers, while surface charges are the dominant factor in forming the zeta potential (Howard and Lekse 2017).

2.2 Zeta potential

When clay particles are immersed in an electrolytic solution like water, the surface can become charged by ionization or dissociation of surface groups or by adsorption of ions from the solution onto a previously uncharged surface (Dąbrowski 2001). These charges will be balanced by oppositely charged ions at the clay surface and in a swarm of ions in solution, which is called the electric double layer. The electric double layer is composed of two parallel layers. The inner layer, called the Stern layer, consists of ions that are strongly bound to the surface electrostatically, while the outer layer that is more loosely associated is known as the Gouy-Chapman layer or the diffuse layer (Vogel 2012).

The zeta potential is defined as the electric potential at the shearing plane outside of the Stern layer (Figure 2.3; Glawdel and Ren 2014). Therefore, the zeta potential is the potential difference between the dispersion medium and the stationary layer of fluid attached to the dispersed particle, rather than a measurement of the Stern potential or surface potential.

Although the concept of zeta potential is important in colloid chemical theory, it has not been used widely in frozen soil research; however, zeta potential is a critical feature of clay minerals, since it partly describes the stability of the colloidal dispersion and the type of micro-aggregates the clay minerals will form (Heagler, Jr. 1964; Lambe 1953). For example, the presence of divalent cations in the Stern layer of a negatively-charged surface neutralizes the mineral surface charge better than monovalent cations, resulting in a higher (less negative) zeta potential and a thinner diffuse layer (Grim 1958). Clay particles with higher zeta potential can approach each other more closely since there is little electrostatic repulsion of the like-charged

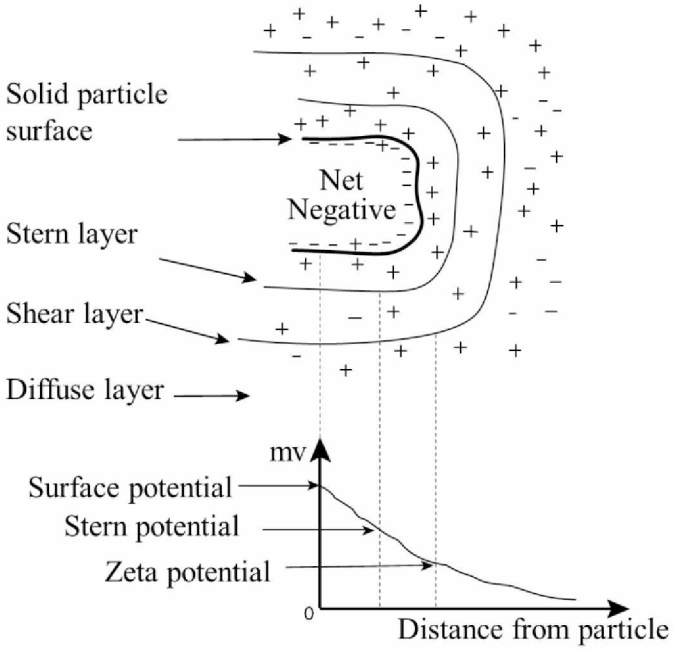

Figure 2.3. Zeta potential and idealized charge distribution of cations and anions around the charged soil particle in solution (adapted from Kaya and Yukselen, 2005).

diffuse layers (Figure 2.4a). These conditions favor edge-to-face electrostatic bonding, resulting in particle aggregation and a fabric consisting of randomly-oriented particles (Heagler, Jr. 1964; Hillel 1980). This fabric type generally results in a relatively high permeability (Aydin et al. 2004). Conversely, if monovalent cations dominate the Stern layer, there is a lower (more negative) zeta potential and a thicker diffuse layer. In this case, there will be strong repulsive interaction among the clay particles, preventing aggregation and resulting in a dispersed soil fabric with low permeability (Figure 2.4b; Aydin et al. 2004; Heagler, Jr. 1964).

2.3 X-ray diffraction (XRD) and texture

The x-ray has long been used to analyze clays qualitatively and quantitatively (e.g., Ross and Kerr 1931; Gruner 1934; Clark and Reynolds 1936; Bradley et al. 1937; Bradley 1940; Alexander and Klug 1948; Brindley 1961; McEwan 1961). The principle uses reflections of three-dimensional planes in the crystal, which are called scattering planes, lattice planes, or Bragg planes. If Bragg's law is satisfied (as shown in Figure 2.5), then constructive interference happens and results in a reflection peak. Bragg's law can be written as:

$$2d \sin \theta = n\lambda \qquad \text{(Equation 2.1)}$$

where the scattering angle, θ, is defined as the angle between the incoming x-ray and the scattering plane, d is the interplanar spacing, n is an integer number of the neighboring planes through which the x-ray traveled, and λ is the wavelength of the x-ray.

The XRD method uses an x-ray diffractometer to record the beam of incident x-rays that are diffracted by crystal planes. The basic parts of an XRD device are the x-ray tube generator and a detector to capture the diffractions. In the experiment, the sample is placed in the center between the source and the detector. Consider the example of a clay sample that is composed of four different minerals with random particle orientations (Figure 2.6). If Bragg's law is satisfied,

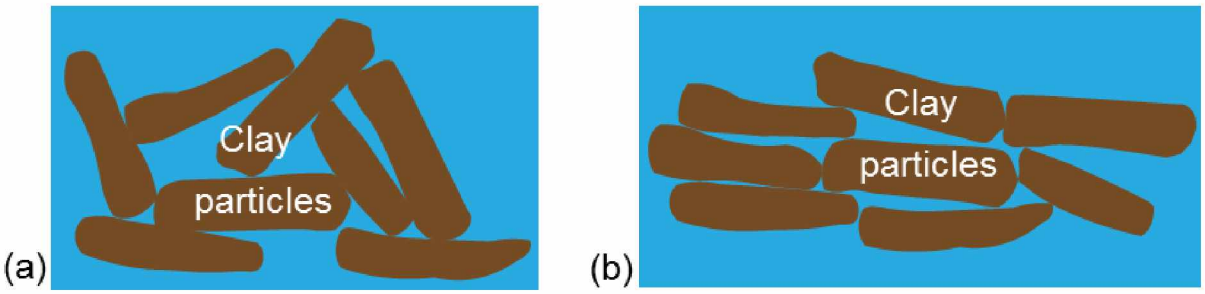

Figure 2.4. Clay particle structures that result from different zeta potentials (not drawn to scale): (a) a flocculated structure with higher permeability; and (b) a dispersed structure with lower permeability.

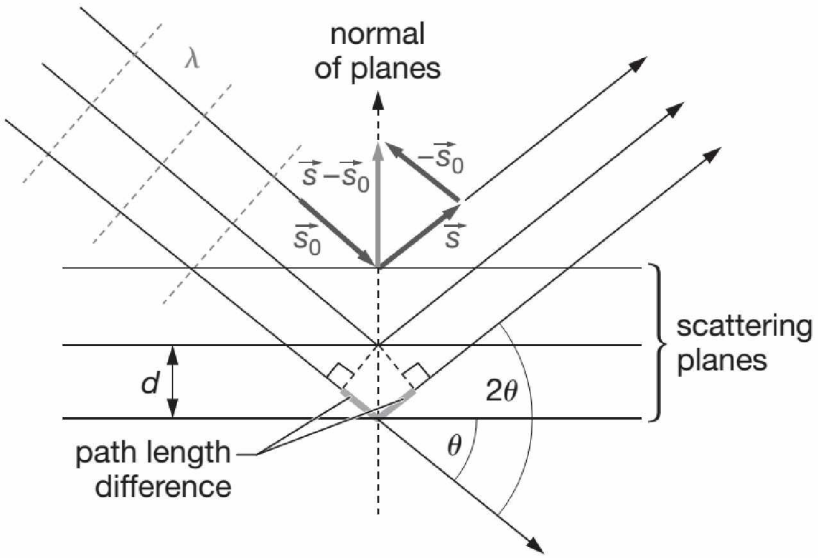

Figure 2.5. Schematic diagram of diffraction in the Bragg condition (taken from Girolami 2015).

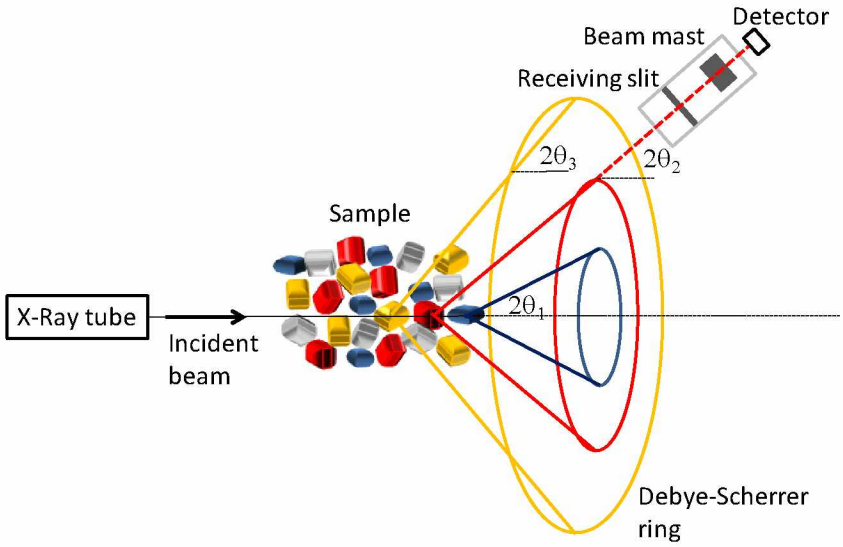

Figure 2.6. Schematic of x-ray diffraction through random power. Four colors represent clay particles with four imagined orientations. Three (blue, red, and yellow) are at the right angles ($2\theta_1$, $2\theta_2$, and $2\theta_3$, respectively) to satisfy Bragg's law, whereas the gray-colored particles are at an orientation where Bragg's law is not satisfied.

the diffraction beam will produce a high intensity that can be captured by the sensor at the position of 2θ, while at other angles, the detector can only receive noise or background signals, which appear as low intensities. The reflections at the angle of 2θ to the incident beam in 3-dimensional (3D) space form cone shapes, which intersect a flat photographic plate as circles, known as Debye-Scherrer rings or simply as Debye rings. Debye, Scherrer, and Hull invented the camera to capture these rings during the early research into powder diffraction (Debye 1915).

If the randomly-oriented clay powder is evenly distributed not only in the directions illustrated in Figure 2.6, but in all directions, the results will include high-intensity diffracted beams that satisfy Bragg's law. If the clay particles have a preferred orientation, some of the high-intensity diffractions will not be captured by the sensor, because of a lack of particles oriented at that specific angle. For example, if all of the particles in Figure 2.6 were oriented the same as the red particles, then the only diffraction beam that could be produced is in the $2\theta_2$ direction, and only the red Debye ring would be detected. In this case, the blue and yellow rings at the positions of $2\theta_1$ and $2\theta_3$ would disappear and not be captured by the detector.

Another deciding factor is the d-spacing in the Bragg condition, which is the distance between the scattering planes, lattice planes, or Bragg planes. The plane in the crystal is defined by the coordinates (hkl) where h, k, and l must be integers and are called Miller indices (Girolami 2015). There are two equivalent ways to define Miller indices. Using a perfect cubic structure as an example, the (hkl) denotes a plane that intercepts at three points: 1/h, 1/k, and 1/l (Girolami 2015).

The common XRD method used to characterize and quantify the orientation of clay particles is a pole figure (Figure 2.7), which is a stereographic projection of the orientation of objects in space. Traditional pole figure measurements are made by recording the intensity of a

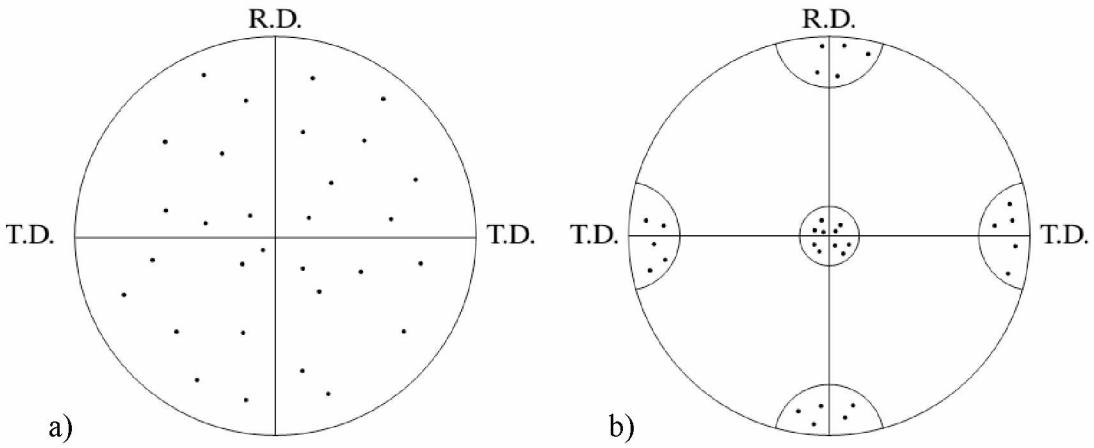

Figure 2.7. Pole figures of (001) for two imaginary sheet materials: a) random orientation with random strong deflection; and b) near-perfect preferred orientation with high intensity deflection distributed together. R.D. is rolling direction and T.D. is transverse direction (taken from Cullity and Stock 2013).

given Bragg reflection as a function of rotation and tilt of the sample (Cullity and Stock 2013). In the situation of preferred orientation, the deflection of those lattice planes that satisfy Bragg's law tend to gather in a pattern rather than having a random or even distribution. During the measurement, the sheet specimen sample is initially fixed in a special holder and rotated about two axes (Figure 2.8). The angle α measures the amount of rotation about the diffractometer axis, which is zero when the sheet bisects the angle between the incident and diffracted beams. When α is zero, the rolling direction is vertical and coincident with the diffractometer axis. The angle δ measures the amount by which the sheet is rotated in its own plane. When δ is zero the transverse direction is horizontal (Cullity and Stock 2013).

Hydration and dehydration can absorb or release water into or out of clays, changing the amount of free water in the soil. Figure 2.9 illustrates an example of water entering into the interlayer of montmorillonite. If one layer of water molecules enters the interlayer, the distance can increase to 12.5 angstrom (Figure 2.9b); if two layers of water enter, the distance can increase to as large as 15.2 angstrom (Figure 2.9c). The interlayer distance plus the thickness of a single aluminosilicate layer constitutes basal spacing (Varadwaj and Kulamani 2013). If increased basal spacing causes swelling, the corresponding scatter angle will decrease and be captured using XRD. The space and the bonding force within the interlayer determine the clay swelling capacity. If the layer charge is large, and the layers are linked through hydrogen bonding such as in kaolinite, hydration or dehydration is minimal and the clay demonstrates weak or no swelling capacity. Changing the basal spacing will change the 2θ of the (001) and thus the (00n) reflection in the pole figure.

The influence of freezing and thawing on the orientation of clay particles is not well-understood. Previous studies focused on mechanisms producing preferred mineral orientations

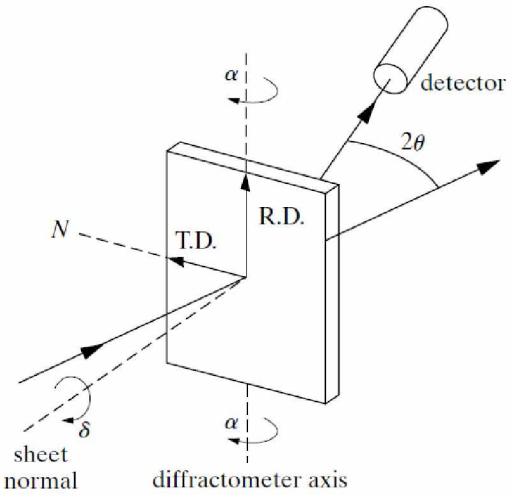

Figure 2.8. Angular relationships in the transmission method showing the different angles (taken from Cullity and Stock 2013).

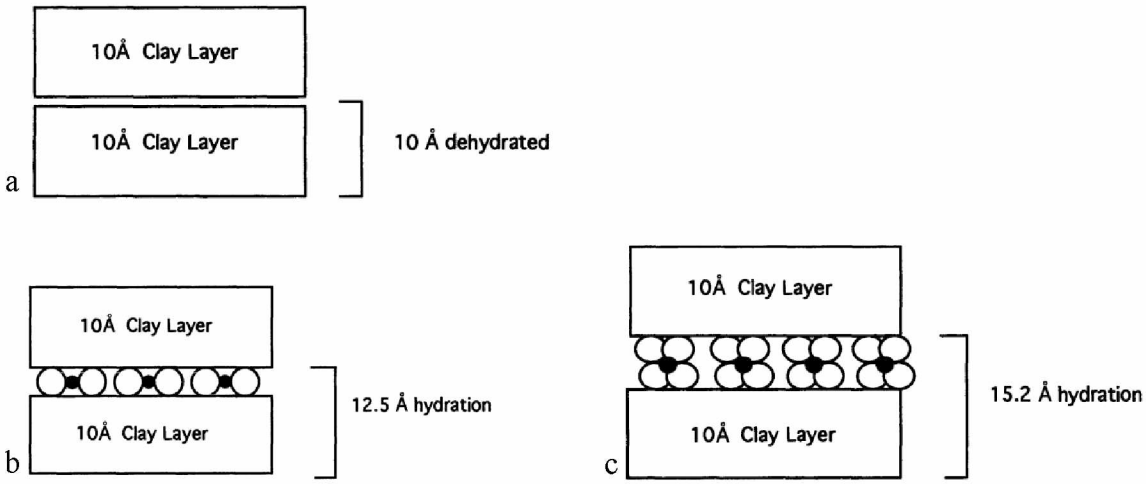

Figure 2.9. Hydration states of two 2:1 layers of montmorillonite with a layer of water in between, formed around exchangeable cations. The thickness of the combined material is indicated for each state of "hydration": a) no hydration, b) one water molecule layer enters into the interlayer; c) two water molecule layers enter into the interlayer (taken from Velde 1995).

include studies on compaction, strain, and fluid-rock interactions (Buatier et al. 2012), and fault gouge (Haines et al. 2009). Some studies have been conducted, however, on the change of basal spacing with temperature. For example, Ahlrichs and White (1962) measured the migration of interlayer water molecules out of bentonite gels to nearby ice crystals, thus reducing the interlayer thickness, and Norrish and Rausell-Colom (1962) also found that the interlayer spacing of montmorillonite gel dropped during freezing and drying. Svensson and Hansen (2010) demonstrated that freezing and thawing changed the basal spacing of Ca^{2+}-treated montmorillonite, influencing the clay texture, and Morodome and Kawamura (2011) used *in situ* XRD to demonstrate that temperature has a strong influence on the basal spacing due to hydration and dehydration of cation-treated montmorillonite.

3. MATERIALS AND METHODS

3.1 Materials and equipment

I tested five clay minerals – montmorillonite, kaolinite, illite, illite-smectite, and chlorite obtained from the Source Clay Repository (Purdue University, West Lafayette, IN) – and a heterogeneous soil sampled from the Copper River Basin, about 5km south of Glennallen, Alaska. The heterogeneous soil (referred to herein as Copper River clay) is classified as a lean clay (CL) using the Unified Soil Classification System. As my work was part of a larger research project, the soil samples already were prepared for different stages of that research; however, I summarize the sample preparation here for completeness.

The illite, illite-smectite, and chlorite were available only in the form of rock chips. These samples were processed first to obtain silt- and clay-sized particles, by gently crushing with a rubber-tipped pestle and a mortar, and then processed in a ball mill, until all particles passed through a US No. 200 (75μm) sieve.

Next, four cation treatments (Ca^{2+}, Mg^{2+}, Na^{+}, and K^{+}) for each of the six soils were prepared, with a fifth sample remaining "untreated" for each soil. For each cation treatment, 40g of soil was mixed with 1L of a 1.05M solution of salt (e.g., $CaCl_2$, $MgCl_2$, NaCl, or KCl). The mixture was divided between two 1L plastic bottles and agitated for two days on a shaker table to ensure cation exchange. The chloride was repeatedly flushed from the soil-brine mixture using Buchner filter funnels and distilled, deionized (DI) water, repeating this rinsing process until the electroconductivity of the effluent measured approximately 10μS. The Na^{+}- and K^{+}-treated montmorillonite, illite, illite-smectite, and Copper River soils demonstrated such low hydraulic conductivity that the DI water would not pass through the clay in the funnel. For these samples, the excess chloride was removed through dialysis. Each sample was transferred into

dialysis tubing, which was suspended in a 600mL beaker and submerged in DI water. The electroconductivity was measured every 24h, and the water was replaced when the electroconductivity became constant. This process was repeated until the electroconductivity was less than 20μS.

Once all the cation treatments were complete, the size of each treated sample was reduced further using a micronizer (McCrone Micronizing Mill, New York, NY), and finally the smallest clay-sized particles were collected using a standing water column procedure. This resulted in samples with grain sizes of 2μm or less. In some cases, the soil particles were centrifuged to collect the supernatant fluid. After drying, the samples were ready for zeta potential measurements.

The sample preparation for the XRD measurements required a few more steps. Each of the soil samples was mixed with deionized water to form a soil slurry, which then was consolidated at 75kPa. Two small cores were sampled from each consolidated soil, using a 4-cm long coring tool with an inside diameter of 1.3cm. These samples were frozen quickly using liquid nitrogen. One of the cores was used for unfrozen water content measurements as part of the larger research project. I prepared part of the second core for XRD measurements, cutting a 2- to 5-mm long cylinder from the end of each core. These frozen, soil cylinders were placed into a freeze dryer to dehydrate while still retaining the clay structure. Once dehydrated, I glued each sample onto a 3cm by 5cm rectangular glass plate, which I placed onto the XRD stage using double-faced adhesive tape.

3.2 Methods for zeta potential research

I used a ZetaPlus Zeta Potential Analyzer (Brookhaven Instruments, Holtsville, NY) to measure the zeta potential (Figure 3.1a). The ZetaPlus system applies an electric field via an electrode to the liquid within a cuvette (Figure 3.1b), which causes the charged particles in a dilute suspension to move to the oppositely charged pole (Figure 3.2). Using user-supplied or calculated input parameters for fluid type (including viscosity, refractive index, and dielectric constant), temperature, particle size, and pH, and by measuring the direction and velocity of the particle movement via a laser beam (Figure 3.1c), the device's software calculates the electrophoretic mobility (U_E). The Smoluchowski approximation is used to calculate U_E (Equation 3.1) for a suspension with particles larger than 0.2μm and an ionic strength equal to or greater than 1mM (Brookhaven 2010):

$$U_E = \frac{\varepsilon \cdot \zeta}{\eta} \qquad \text{(Equation 3.1)}$$

where ε is the dielectric constant, ζ is zeta potential, and η is fluid viscosity. Using the Smoluchowski approximation yields results with 20% error (Brookhaven 2010). Prior to any testing, I calibrated the analyzer using a 92nm Duke reference standard for particle size, and a BI-ZR3 standard (-53 ±5 mV) provided by Brookhaven, Inc. for the zeta potential. The instrument yielded results within 20% error of the reported zeta potential values.

The samples were tested using two different fluid compositions. First, I tested the samples in a 1mM solution of $CaCl_2$, $MgCl_2$, NaCl, or KCl, with the cation of the solution matching the cation treatment. For the untreated samples, I used the 1mM KCl solution as the fluid. Each solution was run through a 0.45μm filter before use, and I triple-rinsed each cuvette with the appropriate 1mM solution prior to adding the sample, to eliminate dust particles. Next,

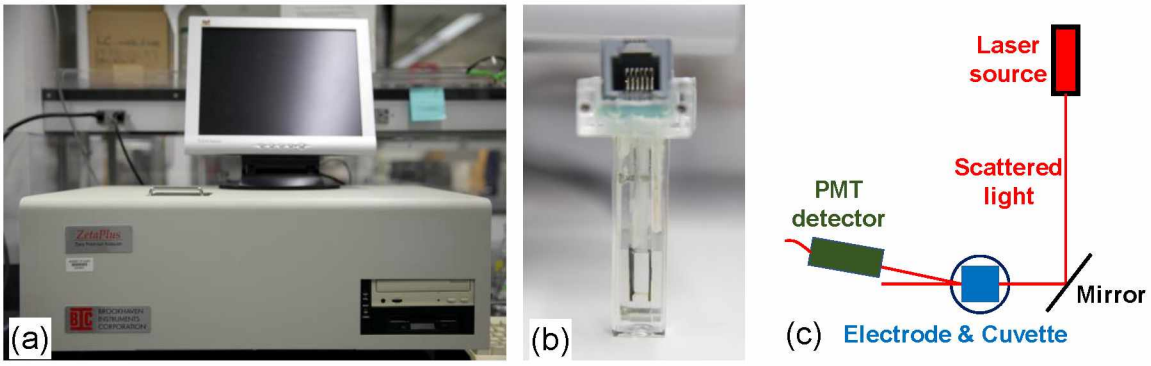

Figure 3.1. Illustrations of the equipment used to measure zeta potential: (a) ZetaPlus Zeta Potential Analyzer and (b) electrode inserted into a cuvette; (c) conceptual sketch of the ZetaPlus system (modified from Brookhaven 2010).

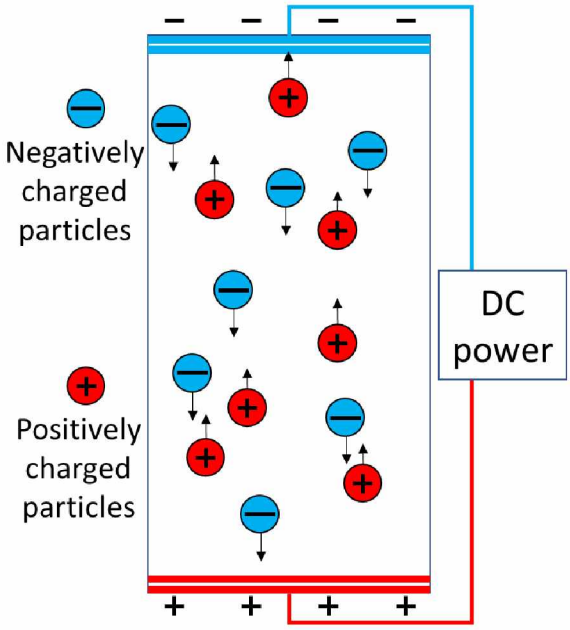

Figure 3.2. Charged particles move towards the oppositely-charged pole of the applied field in the solution.

I prepared a 0.1 mg/mL suspension of each sample, mixing with a sonicator, and then allowing it to rest for a minimum of 30 min prior to testing to allow larger particles to settle. During this time, I measured the pH of the suspension. I placed the cuvette into the analyzer and determined its particle size at room temperature (i.e., 20°C). As the second fluid, all the samples were tested in the supernatant mother liquor prepared during the standing water column procedure.

For both supernatant and 1mM fluid, I measured the zeta potential for each sample at 20, 15, 10, and 6°C; Table 3.1 is a summary of the input parameters used in the analyzer software. For these measurements, the testing temperature of the analyzer was achieved using its internal heating/cooling assembly, typically requiring 15 min to reach temperature stability. For the 20°C and 15°C tests, no additional heating or cooling was required for the electrode assembly and sample. For the 10°C and 6°C tests, however, I immersed the cuvette and electrode assembly into an external thermal bath for 10 min to reach the required temperature. The electrode assembly then was transferred to the analyzer for testing. For each sample, I ran three suites of 10 runs; thus, each result presented here is the average of 30 individual measurements.

Subfreezing tests were conducted only using the 1mM fluid. For these tests, I disabled the analyzer's internal heating/cooling assembly, and moved the entire system into a cold room set at -8°C. To increase the thermal stability of the device, I placed it into a 7-cm thick extruded polystyrene box, which eliminated the cyclical temperature fluctuations typical of cold rooms. The analyzer reached an equilibrium temperature of -1°C (± 0.5°C) after running for three hours. For these tests, I immersed the cuvette in the thermal bath set at -1°C for 10 min prior to testing and for an additional 2 min between measurement suites.

For the subfreezing tests, I added 1.25% ethanol (by volume) to the liquid to lower the freezing point. Prior to the subfreezing testing, I compared the zeta potential measurements with

Table 3.1. Viscosity, refractive index, and dielectric constant of zeta potential solution at testing temperatures. DI water was used for above-freezing temperatures, and a 1.25% ethanol-water solution was used at -1°C. Values for above-freezing temperatures were taken directly from the analyzer software (Brookhaven 2010); values for -1°C were interpolated from several sources.

Temperature (°C)	Viscosity (mPa·s)	Refractive Index (RIU)	Dielectric Constant $F \cdot m^{-1}$
20	1.002	1.331	80.37
15	1.139	1.331	82.24
10	1.307	1.332	84.16
6	1.472	1.332	85.72
-1	1.872	1.335	87.77

and without the ethanol solution for all cation treatments of montmorillonite and illite. The results indicated differences less than 15%, which was within the reported accuracy (20%) of the ZetaPlus system. Adding ethanol changed the viscosity, refractive index, and dielectric constant of the fluid. Although no published work specifically tested these parameters for a 1.25% ethanol-water mixture at -1°C, several papers (Bloomfield and Dewan 1971; Nowakowska 1939; Simmonds 1919; Weirong and Lempe 2006; Wyman 1931) reported work systematically done for a broad range of concentrations and temperatures. I first used these data to interpolate the viscosity (Table 3.1), refractive index, and dielectric constant of the solution at each given temperature for 0.499% ethanol by weight, then interpolated again to determine these parameters at -1°C. Table 3.2 is a summary of the interpolated results, and finally, Figure 3.3 illustrates the interpolation results of viscosity for the 0.499% ethanol mixture by weight.

In order to isolate the temperature effects on zeta potential, I also measured the zeta potential's response to changes in pH for the suite of montmorillonite samples. Using HCl or NaOH to reach the desired pH, I measured the zeta potential of 0.1 mg/mL suspensions at pH values ranging from 1.5 to 9 at 20°C.

3.3 Methods for XRD research

I used a PANalytical X'PERT device (PANalytical B.V, Almelo, Netherlands) for the XRD measurements (Figure 3.4). An XRD measurement for a pole figure of a sample can be divided into two steps. The first step is a peak find, also called an absolute scan, to find the specific peak for the Miller indices. The second step is a texture measurement to determine the diffraction pattern at the specific peak previously found in the first step.

An absolute scan also is used to scan a powder to locate the peak locations in the diffraction pattern to identify an unknown sample. The resulting peaks may be slightly shifted as

Table 3.2. Interpolation of the water-ethanol mixture's viscosity as a percentage of alcohol by weight at different temperatures; 1.25% of ethanol by volume is equal to 0.499% by weight. The data for above-freezing temperatures are from Simmonds (1919).

Temp.	% by weight									
°C	0	10	20	30	40	50	60	70	80	0.499
0	1.792	3.311	5.319	6.94	7.14	6.58	5.75	4.762	3.69	1.812
10	1.308	2.179	3.165	4.05	4.39	4.18	3.77	3.268	2.71	1.336
20	1.005	1.538	2.183	2.71	2.91	2.87	2.67	2.37	2.008	1.020
30	0.801	1.16	1.553	1.87	2.02	2.02	1.93	1.767	1.531	0.814
40	0.656	0.907	1.16	1.368	1.482	1.499	1.447	1.344	1.203	0.667
50	0.549	0.734	0.907	1.05	1.132	1.155	1.127	1.062	0.968	0.558
60	0.469	0.609	0.736	0.834	0.893	0.913	0.902	0.856	0.789	0.476
70	0.406	0.514	0.608	0.683	0.727	0.74	0.729	0.695	0.65	0.412
-1	---	---	---	---	---	---	---	---	---	1.872

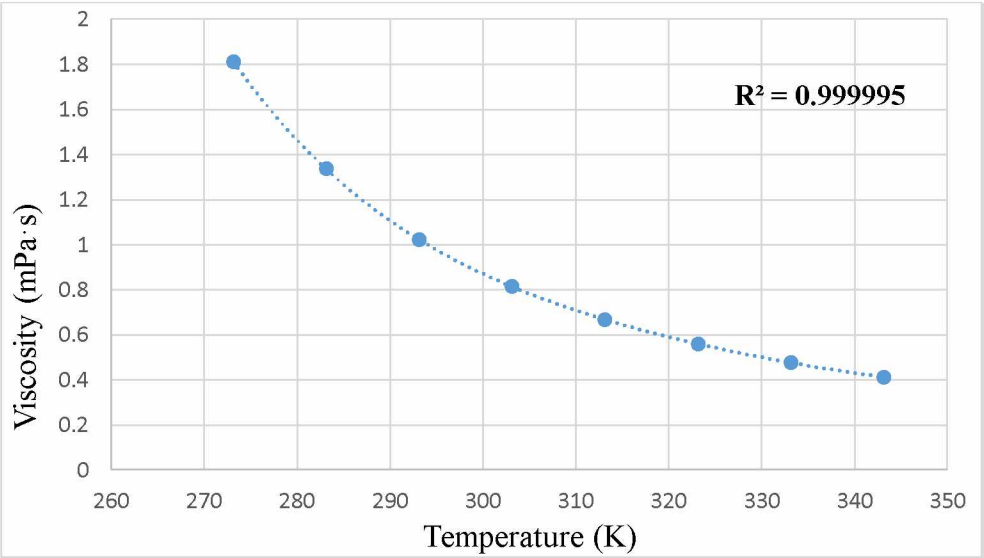

Figure 3.3. Interpolation of viscosity with 1.25% ethanol for subfreezing temperatures.

Figure 3.4. Photograph of the PANalytical X'Pert Pro XRD device.

compared to the International Center for Diffraction Data (ICDD) standard, because of small errors in the alignment or running of the device. First, I placed the sample between the x-ray source and the detector, and then used the lower current (45kV voltage, 20mA current) to align the sample in the X, Y, and Z directions to ensure that the x-ray travel path was in the center of the specimen surface. I selected a 2θ range starting from 4° to avoid the direct exposure of the sensor to the x-ray and stopped at 40° because of the weak intensity at large angles and the small d-spacing at this range.

I used the HighScore Plus software from PANalytical to analyze the results. Since I already knew the type of clay I was scanning, I only needed to compare my results to a small number of patterns from the large ICDD database included with HighScore Plus. The first step was to confirm that the peaks in my sample had the same 2θ locations as the database peaks. Next, I needed to determine the correct polytype for the specific clay. Due to dehydration of some samples, the peaks at (00n) (especially at (001)) varied. It is important to identify which reflection results correspond to which peaks as a standard in the diffraction pattern (hkl surface). Finally, since the 2θ values determined in the absolute scan are representative of the background level near each peak, I used these values for the background measurement in the subsequent texture measurement. Knowing the 2θ value of the peak of interest, d-spacing can be determined using either Bragg's law or the software. If the peak at (001) is the confirmed (d_{00n}), then the d-spacing of (00n) is calculated by d_{001}/n. Since the Copper River clay was a heterogeneous soil, the peaks were the result of a mixture of smectite, illite, and chlorite. This made it hard to identify the reflection pattern, potentially introducing uncertainty into the texture measurement with an incorrect pattern.

If the loading and alignment of the specimen are correct and the absolute scan is successful, then the texture measurement can be performed with the same XRD setup. For these measurements, I first moved the detector to the 2θ with the proper (hkl) reflections of interest and chose the angles near the peaks from the absolute scan to perform the background measurement. Typically, one texture measurement and one background measurement can be carried out as a pair; a batch can be setup for a pair or several pairs, allowing multiple measurements to be performed automatically.

The texture measurement requires moving the sample rather than moving the sensor during the absolute scanning (Figure 3.5). The sample is rotated first in the χ axial direction usually stopped at a step of 5°, and then rotated in the ϕ direction (0-360°) continuously. Then the sample is moved to the next step of χ direction and a 360° scan is performed in the ϕ direction, until all the scanning from 0 to 85° in the χ direction is finished. The resulting pole figure will record the scanning information for all the ϕ directions for the χ angles from 0° to 85° usually at a step of 5°.

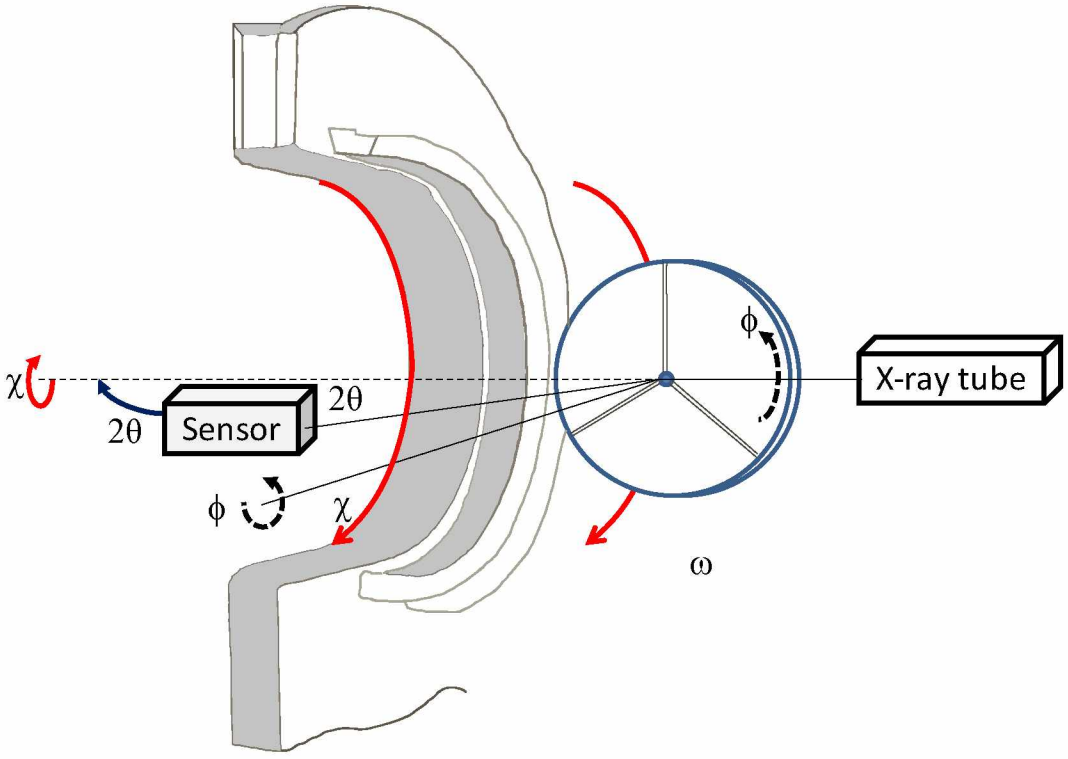

Figure 3.5. Schematic of conducting a texture scan with a fixed 2θ and sensor position. The sample is rotated first in the χ axial direction, and then rotated in ϕ direction.

4. RESULTS

4.1 Zeta potential results

4.1.1 Zeta potential measurements using the 1mM fluid

The zeta potential results using the 1mM fluid are presented in Table 4.1 and Figure 4.1. The tests demonstrate linear correlations between zeta potential and temperature. For all soils, the two divalent cation treatments (Ca^{2+}, Mg^{2+}) showed similar outcomes and demonstrated higher (less negative) zeta potential. The monovalent cation treatments formed a second group of lower (more negative) zeta potential. The untreated samples typically grouped with the monovalent cation treatments, most likely due to the use of 1mM KCl as the fluid used in testing.

Generally, all treatments demonstrated a negative correlation with temperature; i.e., the zeta potential became more negative with increasing temperature. This trend followed across the 0°C isotherm. In some cases, the temperature effect on the divalent samples was less pronounced. The Mg^{2+}-treated illite-smectite was a good example of this, suggesting that changing temperature did not affect the zeta potential of this treated soil. For this same soil, however, the monovalent treatments demonstrated a strong negative correlation. As another example, all of the montmorillonite treatments demonstrated an overall negative linear correlation with temperature. The Na^{+}-treated montmorillonite, and untreated and Na^{+}-treated chlorite, however, demonstrated an apparent positive relationship for the above-freezing temperatures. The Ca^{+}-treated kaolinite demonstrated a consistent negative trend for the above-freezing temperatures, but the subfreezing reading did not follow this trend. A relatively flat trend was present in the Na^{+}-treated illite. In general, the zeta potential increased at the measured subfreezing temperature.

Table 4.1. Numerical zeta potential results for cation-treated soils in 1mM fluid.

Soil	Temperature (°C)	Treatment				
		Untreated	Ca^{2+}	Mg^{2+}	Na^{+}	K^{+}
Montmorillonite	20.00	-39.14	-11.93	-15.41	-40.57	-39.66
	15.00	-36.95	-12.25	-13.24	-41.83	-39.02
	10.00	-36.27	-10.90	-12.76	-44.87	-38.31
	6.00	-34.66	-10.60	-11.24	-45.08	-37.28
	-1.00	-23.40	-6.89	-6.40	-29.71	-25.21
Kaolinite	20.00	-32.33	-13.33	-14.11	-38.93	-32.32
	15.00	-30.49	-12.91	-11.58	-37.19	-31.30
	10.00	-29.66	-11.70	-9.06	-35.54	-33.37
	6.00	-22.62	-10.24	-10.08	-32.79	-25.16
	-1.00	-23.26	-18.81	-9.33	-34.86	-23.90
Illite	20.00	-34.45	-17.01	-13.80	-32.55	-31.94
	15.00	-31.02	-15.17	-14.68	-29.73	-30.40
	10.00	-28.98	-12.78	-13.48	-28.53	-29.41
	6.00	-26.39	-13.43	-13.64	-26.90	-28.12
	-1.00	-25.66	-10.10	-13.45	-32.57	-24.15
Illite-smectite	20.00	-38.66	-16.82	-12.28	-46.01	-44.38
	15.00	-36.18	-16.78	-14.31	-45.36	-38.70
	10.00	-34.68	-12.98	-14.91	-39.50	-40.24
	6.00	-30.99	-9.94	-14.57	-32.09	-33.93
	-1.00	-22.59	-12.53	-10.95	-32.92	-27.82
Chlorite	20.00	-30.08	-11.29	-13.13	-24.80	-33.85
	15.00	-31.26	-15.39	-14.75	-22.82	-33.73
	10.00	-36.87	-9.95	-11.52	-27.96	-33.30
	6.00	-36.43	-12.30	-10.98	-29.67	-32.26
	-1.00	-20.24	-9.87	-9.29	-27.01	-25.13
Copper River	20.00	-36.47	-15.21	-13.62	-38.94	-43.78
	15.00	-30.09	-14.93	-16.50	-37.20	-35.95
	10.00	-30.36	-12.50	-15.48	-36.48	-38.89
	6.00	-30.59	-9.94	-15.32	-31.49	-40.93
	-1.00	-28.66	-10.72	-9.24	-30.76	-35.74

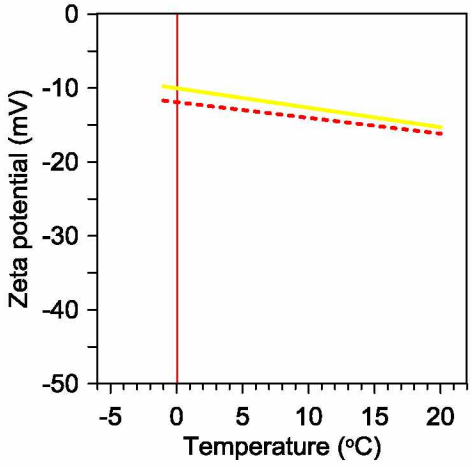

Figure 4.1. Graphical zeta potential results for the cation-treated soils in 1mM fluid: a) montmorillonite; b) kaolinite; c) illite; d) illite-smectite; e) chlorite; and f) Copper River.

4.1.2 Zeta potential measurement using supernatant mother liquor

The effect of temperature on zeta potential is not as pronounced when using the supernatant mother liquor fluid (Figure 4.2). For montmorillonite, illite-smectite, and chlorite, the monovalent cation treatments demonstrated smaller zeta potential values than the divalent cation treatments, similar to the 1mM results. For the remaining samples, however, it is difficult to differentiate the monovalent and divalent treatments, as all treatments demonstrated zeta potentials typically less than -15mV with negligible temperature effects.

4.1.3 Effects of pH on zeta potential and point of zero charge (PZC)

The acid-base zeta potential titration curves (Figure 4.3) indicate that the zeta potential becomes less negative with increasing acidity for all cation treatments. At pH values between 6 and 7 (i.e., at similar pH to the suite of zeta potential tests conducted for the rest of this research), the zeta potential varied little for a given soil treatment. Worrying about the risk of acid eroding the electrode, I did not measure at pH values smaller than 1.5. Although all results trended towards 0mV with the decreasing pH, I was unable to measure the PZC for this soil in this pH range.

4.2 XRD results

4.2.1 Bulk powder scan

I completed pole figure scans of random powder samples for all of the K^+-treated soils. The results were analyzed using the HighScore Plus software to compare with the ICDD database. The montmorillonite, kaolinite, chlorite, and illite samples can be matched with montmorillonite (Reference code: 00-058-2038) (Figure 4.4a), kaolinite-1A (Reference code: 00-058-2004) (Figure 4.4b), chlorite (Reference code: 00-002-0028) (Figure 4.5a), and illite

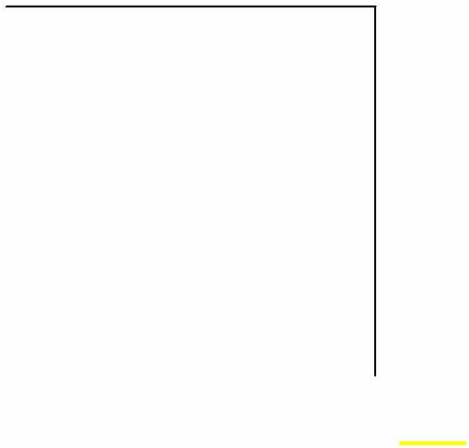

Figure 4.2. Zeta potential results for the cation-treated soils in supernatant fluid:

a) montmorillonite; b) kaolinite; c) illite; d) illite-smectite; e) chlorite; and f) Copper River.

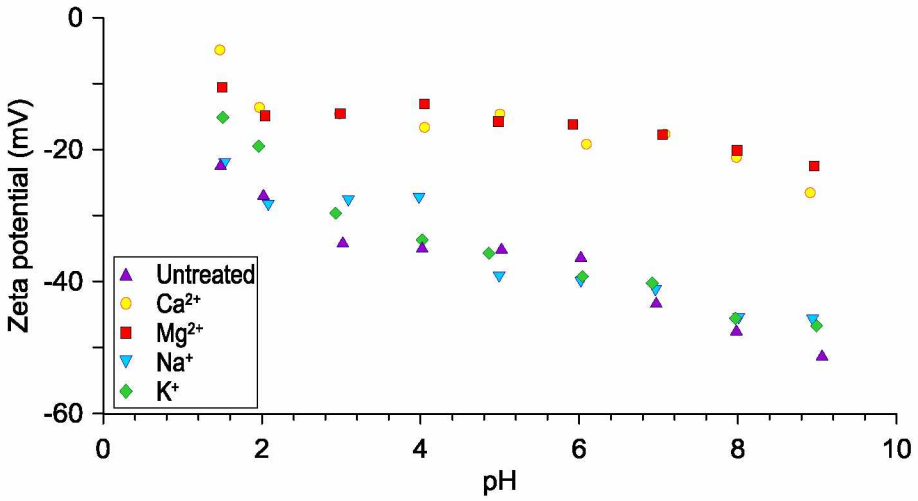

Figure 4.3. Zeta potential results of cation-treated montmorillonite with changing pH values.

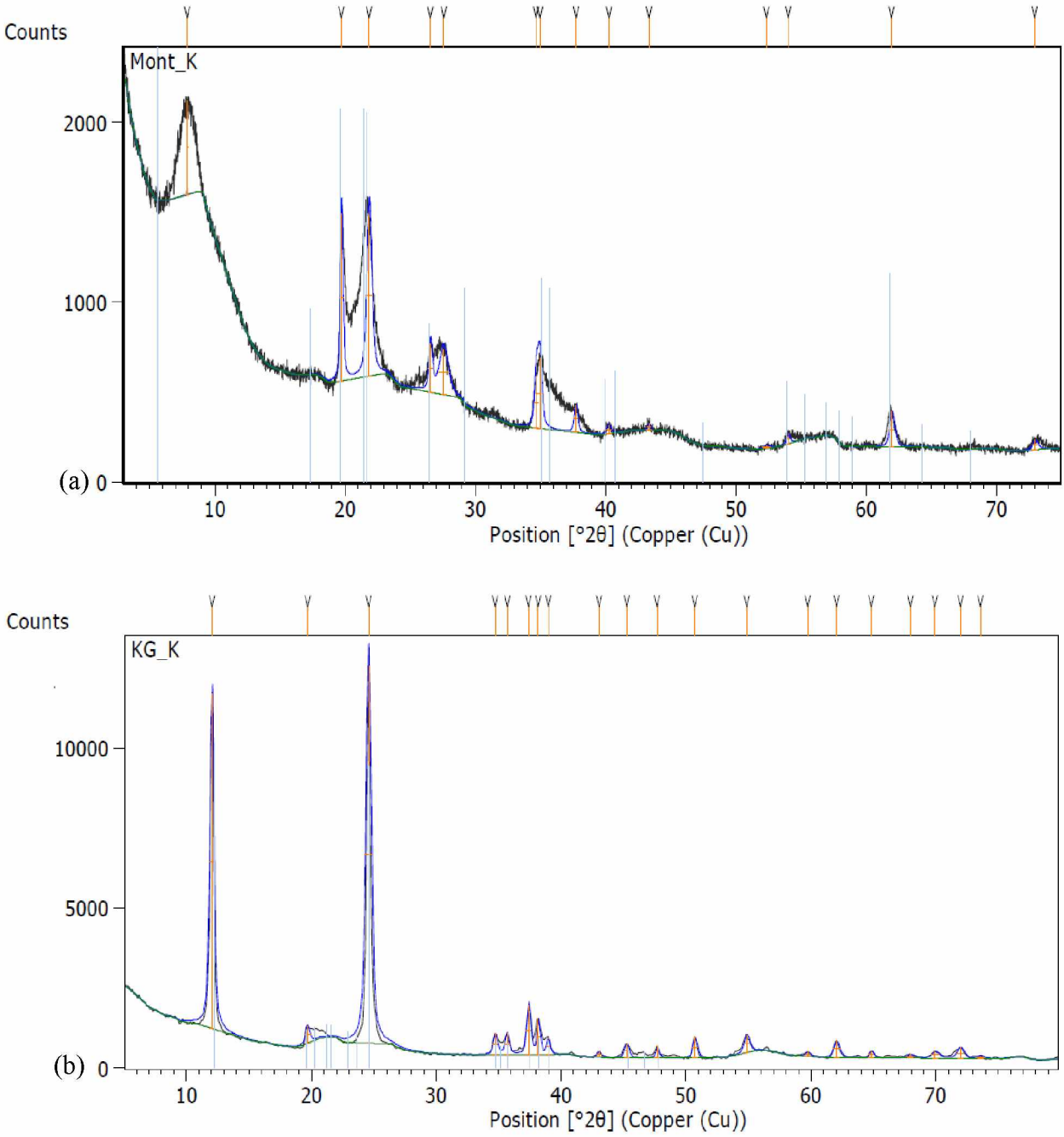

Figure 4.4. Bulk powder scan results for K^+-treated a) montmorillonite random sample, and b) kaolinite random sample. Blue vertical lines indicate the standard pattern for each clay. Orange vertical lines indicate measured peaks.

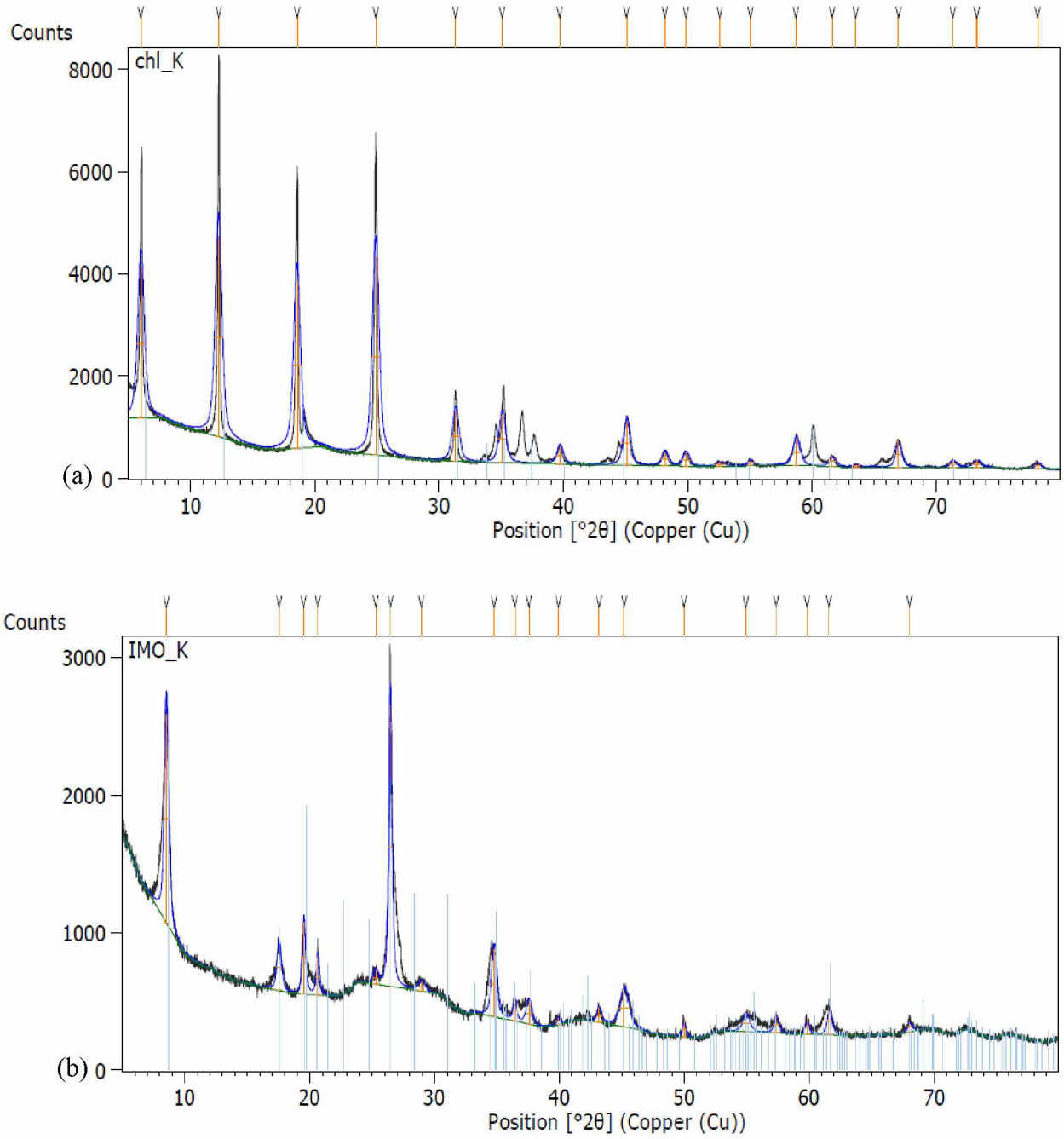

Figure 4.5. Bulk powder scan results for K^+-treated a) chlorite random sample; and b) illite random sample. Blue vertical lines indicate the standard pattern for each clay. Orange vertical lines indicate measured peaks.

(Reference code: 04-017-0520) (Figure 4.5b), respectively. One exception to these matches is that the K^+-treated montmorillonite results indicate the (001) peak shifted to 7.568°, compared with 6.652° from the ICDD standard. The K^+-treated illite-smectite sample (Figure 4.6a) demonstrated a pattern that shares some, but not all, peaks with illite (Figure 4.5b). It also differs from the montmorillonite sample (Figure 4.4a). The Copper River soil (Figure 4.6b) results are more complicated, as they consist of more than one mineral. Previous semi-quantitative XRD analysis indicated that the Copper River soil consisted of chlorite (41%), randomly-ordered mixed-layer chlorite-smectite (30%), illite-smectite (24%), and kaolinite (5%) (Kruse et al., 2018). Next, I compared the random powder scan results with the pellet absolute scan results.

4.2.2 Pellet absolute scans

Pellet absolute scans are used to find the Miller indices for pole figure measurement. I completed pellet absolute scans for selected cation treatments of chlorite, illite, illite-smectite, and kaolinite (Table 4.2), and for the complete suite of cation-treated montmorillonite samples (Table 4.3). As with the random powder results for montmorillonite, kaolinite, illite, and chlorite, I easily matched peaks with the ICDD database using the PANalytical HighScore Plus software.

Most of the peaks were well-matched and displayed no shift or intensity reduction of the (001) or other (00n) peaks for kaolinite, illite, and chlorite when compared with either the random powder results or the ICDD standard. For the montmorillonite and illite-smectite pellet samples, however, I observed a shift or reduced intensity of the (001) peak in the absolute scan for certain cation treatments. The resulting pole figures also demonstrated strong to modest preferred orientation depending on the decreased peak intensity.

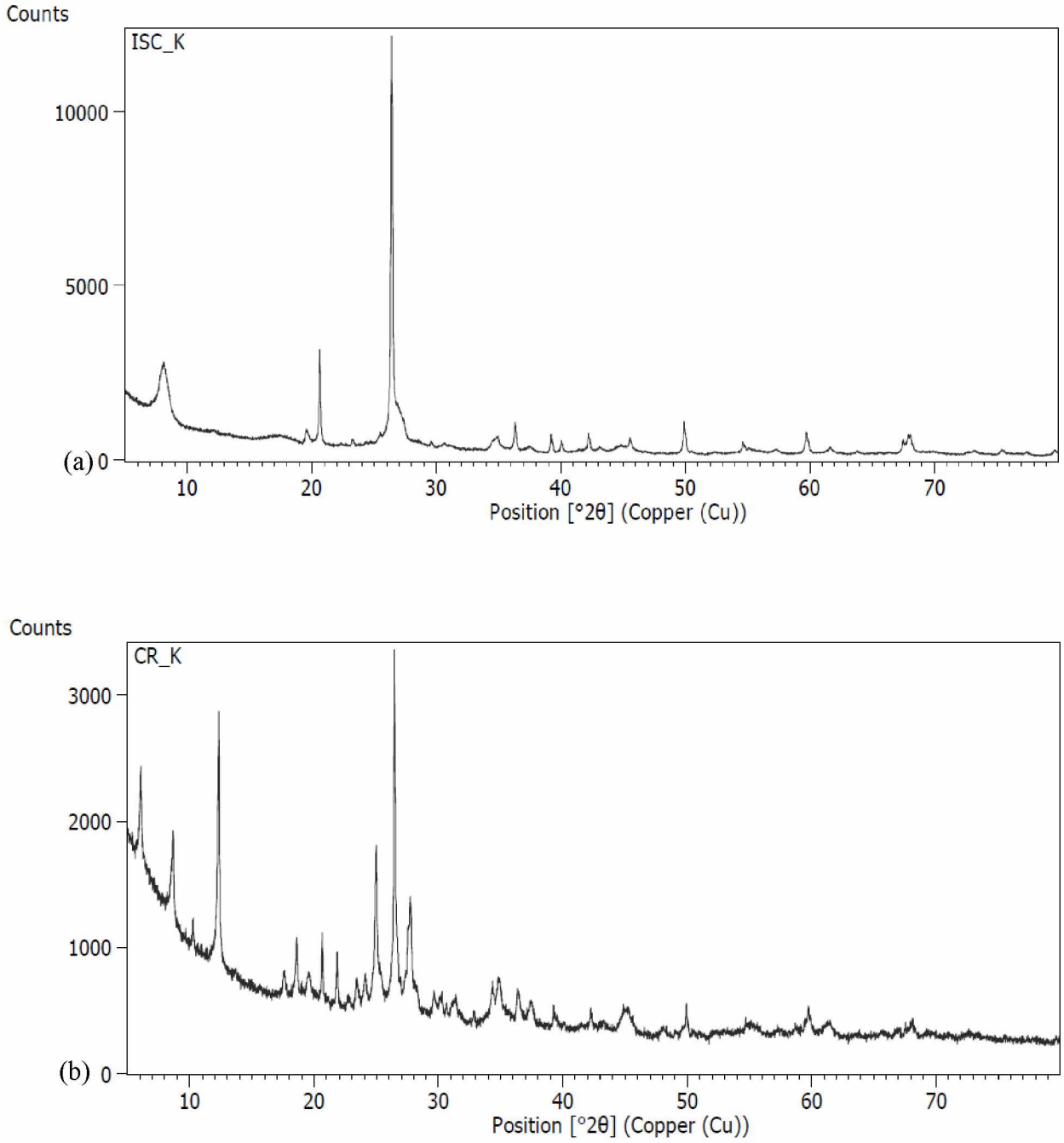

Figure 4.6. Bulk powder scan results for K^+-treated a) illite-smectite random sample and b) Copper River soil random sample.

Table 4.2. Absolute scan results and pole figure measurements performed for chlorite, illite, illite-smectite, and kaolinite samples. "I" stands for peak intensity.

Sample name	hkl	2θ		d-spacing (Å)	I (%)	Mineral name	Rf. code
		Measured (°)	Database (°)				
Chl_Mg	0 0 4	12.5101	12.636	7.0000	80	Chlorite	00-002-0028
Chl_Na	0 0 4	25.1106	25.136	3.5400	80	Chlorite	00-002-0028
Chl_Na	0 0 8	12.4891	12.636	7.0000	80	Chlorite	00-002-0029
Chl_Na	0 0 6	18.7507	18.907	4.6900	80	Chlorite	00-002-0030
CR_Ca	0 0 3	26.6675	26.603	3.3480	64	Illite	04-017-0520
Ill_Untr	0 2 1	34.7392	34.701	2.5830	100	Illite	00-043-0685
Ill_Untr	0 0 6	26.6614	26.603	3.3480	64	Illite	00-043-0686
I/S_K	0 0 3	26.6514	26.604	3.3479	100	Illite	04-017-0520
I/S_K	0 2 2	26.6514	26.604	3.3479	100	Illite	04-017-0520
I/S_Na	0 0 6	26.6404	26.603	3.3480	64	Illite	00-043-0685
I/S_Untr	0 0 3	26.6709	26.604	3.3479	100	Illite	04-017-0520
Kao_Ca	0 0 1	12.4055	12.302	7.1889	75.3	Kaolinite	00-058-2030
Kao_Ca	0 0 2	24.8611	24.845	3.5809	100	Kaolinite	00-058-2030
Kao_Na	0 0 1	12.3477	12.302	7.1889	75.3	Kaolinite	00-058-2030
Kao_Na	0 0 2	24.8718	24.845	3.5809	100	Kaolinite	00-058-2030

Table 4.3. Absolute scan results and pole figure measurements performed on montmorillonite samples and compared to the powder diffraction file (PDF) database. "d" is the d-spacing and "I" is the peak intensity.

h	k	l	Measured 2θ (°)					ICDD database values		
			Untreated	Ca^{2+}	Mg^{2+}	Na^{+}	K^{+}	2θ (°)	d (Å)	I (%)
0	0	1	6.652	6.6864	6.2114	7.2718	7.5534	5.717	15.4459	100
0	0	3	N/A	N/A	N/A	N/A	N/A	17.397	5.0933	15.4
0	2	0	19.8577	19.8622	19.8078	19.8536	19.8582	19.786	4.4834	63.9
1	1	1	21.8666	21.839	21.7906	21.8961	21.8012	21.753	4.0824	61.7
0	2	3	27.6695	27.6927	26.64	27.6695	26.64	26.566	3.3527	15.9
0	0	5	28.3521	N/A	N/A	28.3521	27.5807	29.259	3.0499	26.6

For the montmorillonite pellet samples, all of the cation treatments matched the montmorillonite calcian (NR) sample (Reference code: 00-058-2038). All (001) peaks displayed apparent shifts, suggesting a decreased d-spacing, while I noted only negligible differences for the (020), (-112), and (-202) lattice planes. Peaks at (003) for all the montmorillonite samples and peaks at (005) for Ca^{2+}- and Mg^{2+}-treated samples could not be observed.

As illustrated in Figure 4.7, the K^{+}-treated montmorillonite demonstrated the largest shift for (001) from 5.717° (ICDD PDF data) to 7.553°, and a large intensity reduction. Additionally, the peaks for (003) at 17.397° (ICDD PDF data) and for (005) at 29.259° (ICDD PDF data) also shifted or disappeared. Using the d_{001} of 11.704 at a 2θ of 7.553° and the method summarized in Section 3.1, d_{003} can be calculated as 3.901, and d_{005} as 2.341. Using Bragg's law, the calculated 2θ angles for (003) and (005) are 23.225° and 41.091° (which is beyond the range of these measurements), respectively, as indicated at the top of Figure 4.7. Inspection of Figure 4.7 indicates that no peaks can be observed at these calculated values at (003) and (005).

The pellet absolute scan result for K^{+}-treated montmorillonite has a similar peak at (001) (7.553°) compared with random powder result (7.568°), the difference of which may be negligible, but the intensity for the pellet sample also dropped significantly. This is probably because the preferred orientation in the pellet sample directs the diffraction towards other directions, while the diffraction of random powder can cover all the directions and be captured by the sensor. If the strong intensity can be captured in pole figure, the assumption for preferred orientation could be valid.

The (001) peak for untreated montmorillonite (Figure 4.8) demonstrated a modest shift to 6.652° compared to the ICDD standard and a modest drop of intensity. Similar to the K^{+}-treated

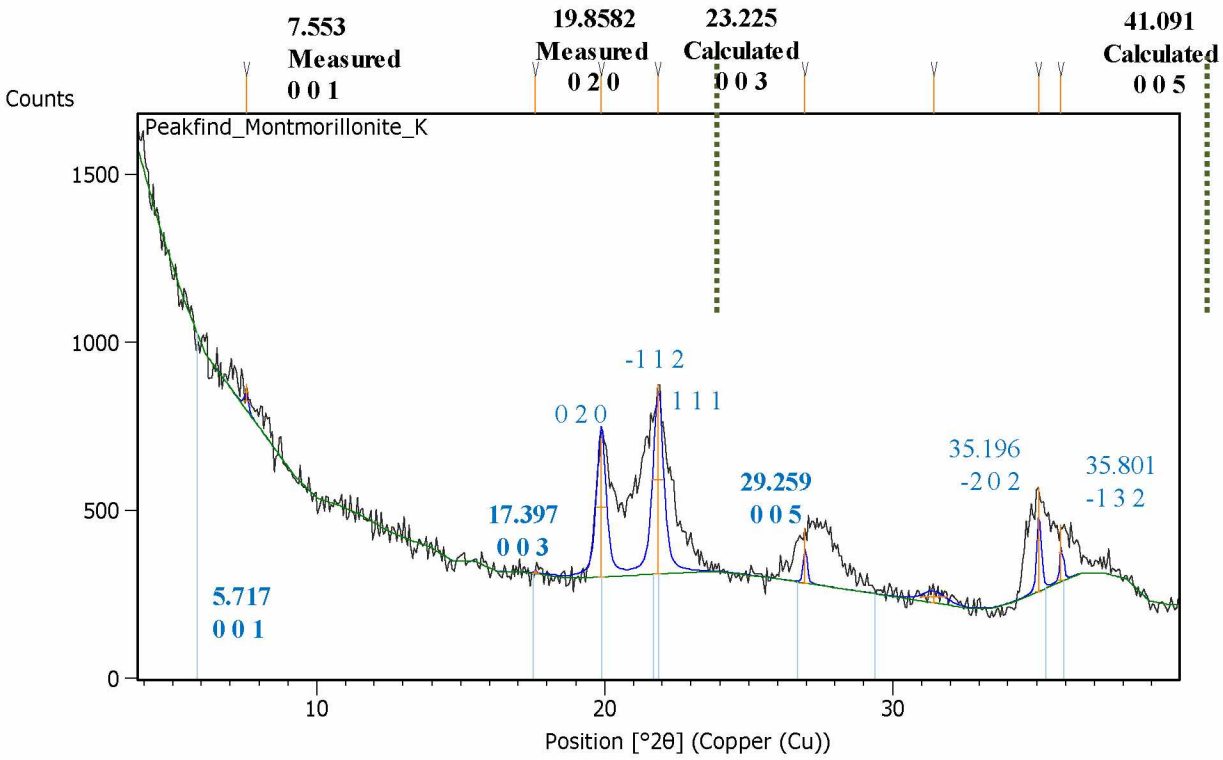

Figure 4.7. Absolute (ω and 2θ) scan results for the K^+-treated montmorillonite pellet sample. Blue vertical lines indicate the standard pattern for montmorillonite (Reference code: 00-058-2038). Orange vertical lines indicate measured peaks. Green dotted vertical lines at the top of the figure indicate the inferred peaks at (003) and (005) calculated using the (001) d-spacing.

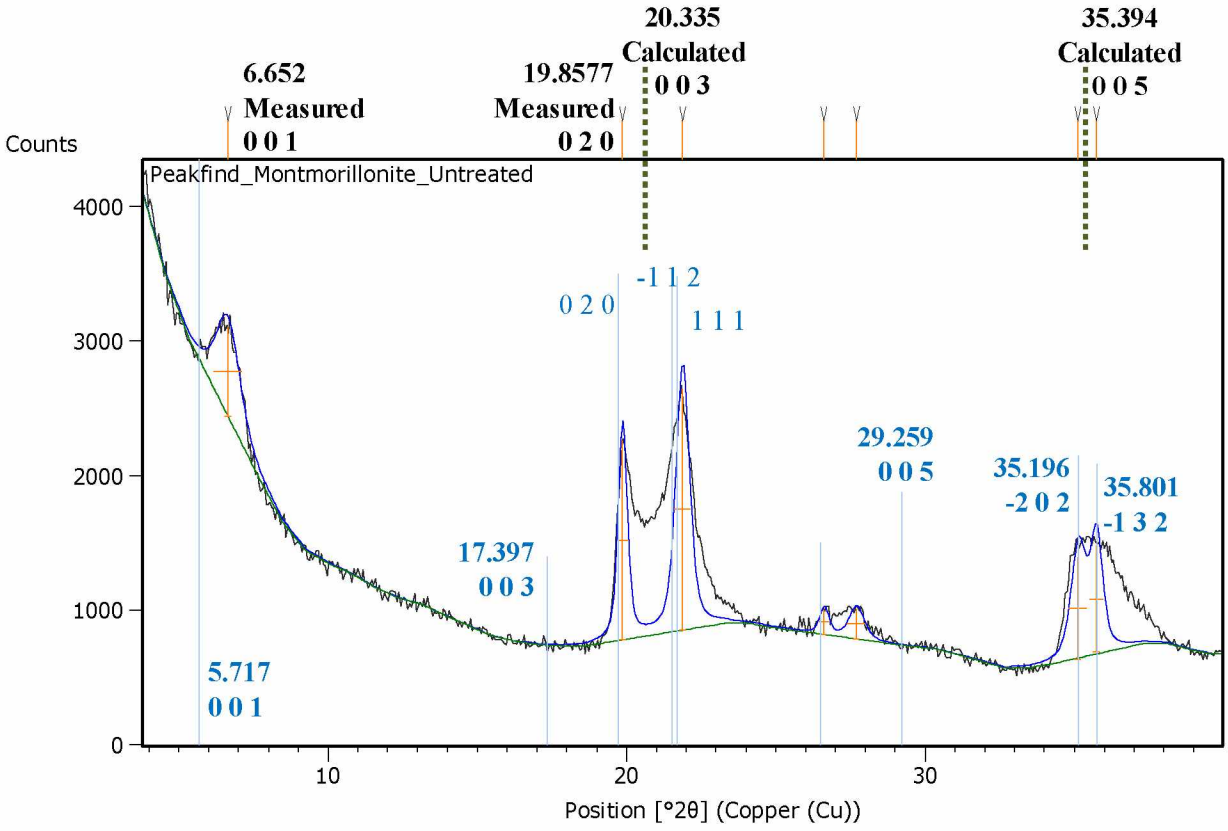

Figure 4.8. Absolute (ω and 2θ) scan results for the untreated montmorillonite pellet sample. Blue vertical lines indicate the standard pattern for montmorillonite (Reference code: 00-058-2038). Orange vertical lines indicate measured peaks. Green dotted vertical lines at the top of the figure indicate the inferred peaks at (003) and (005) calculated using the (001) d-spacing.

sample, no peak was measured at 20.335° for (003) and 35.394° for (005). In contrast, there were perfect matches with the ICDD standard for surfaces not normal to the (00n) planes, as indicated at (020), (-112), and (-202) with strong intensities.

The Mg^{2+}-treated montmorillonite sample (Figure 4.9) also demonstrated a modest shift of the (001) peak to 6.256° with strong intensity. As with the other montmorillonite samples, no peaks were present at 19.080° for (003) and at 33.012° for (005). There were perfect matches with the ICDD standard for surfaces that are not normal to the (00n) planes with strong intensity. The results for the Ca^{2+}-treated (Figure 4.10) and Na^{+}-treated samples (Figure 4.11) were similar to the untreated and Mg^{2+}-treated samples, demonstrating a modest shift and strong to modest intensity at (001). I could not observe peaks at (003) and (005) for any of the treatments, even when the samples had clear peaks at (001). Considering that the d-spacing at (003) or (005) could be shifted because of the shifted (001) d-spacing, no peaks can be observed at the calculated values according to the newly-observed d-spacing at (001).

For the mixed-layer illite-smectite, it is difficult to match all of the peaks with the standard data. I noted that the untreated illite-smectite pellet results are similar to the K^{+}-treated powder results, but they demonstrated an intensity drop in the peak at 8° (Figure 4.6a). The Copper River soil results demonstrated a combination of reflection patterns that could not be easily used for texture measurements. Since I did not find reliable Miller indices information, especially for the single 2θ at the (001) peak that is needed for the pole figure scan, I did not analyze the preferred alignment of the Copper River samples.

4.2.3 Pole figure measurements

The textures measured for montmorillonite were consistent with the absolute scan results. A large reduction in intensity of the (001) peak, as in the K^{+}-treated sample, is accompanied by a

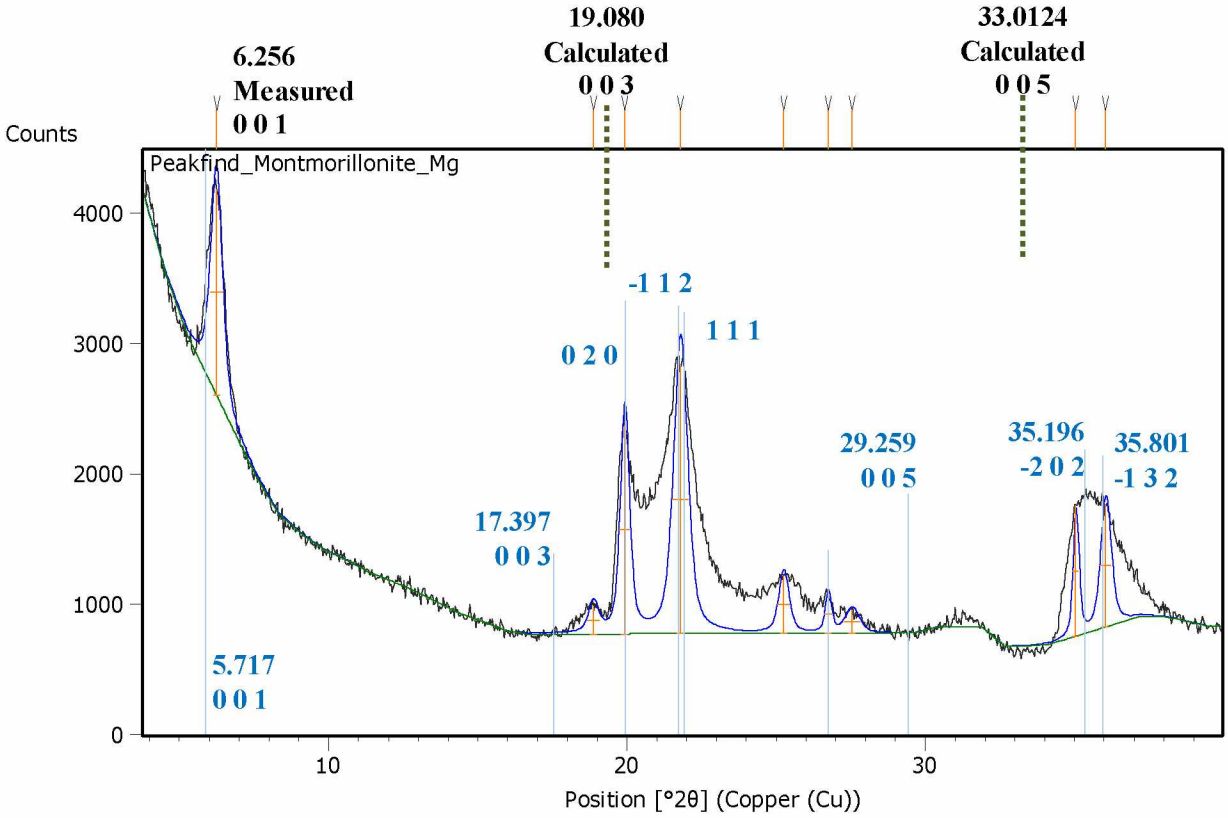

Figure 4.9. Absolute (ω and 2θ) scan results for the Mg^{2+}-treated montmorillonite pellet sample. Blue lines indicate the standard pattern for montmorillonite (Reference code: 00-058-2038). Orange vertical lines indicate measured peaks. Green dotted vertical lines at the top of the figure indicate the inferred peaks at (003) and (005) calculated using the (001) d-spacing.

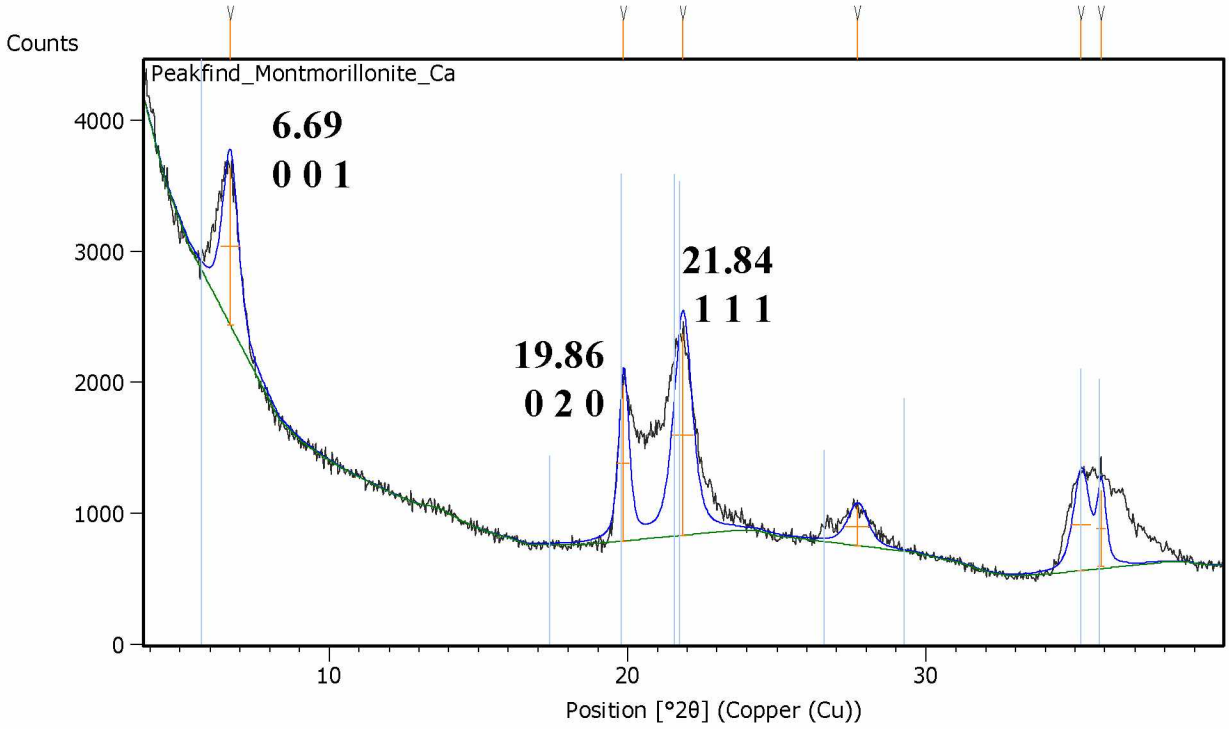

Figure 4.10. Absolute (ω and 2θ) scan results for the Ca^{2+}-treated montmorillonite pellet sample.

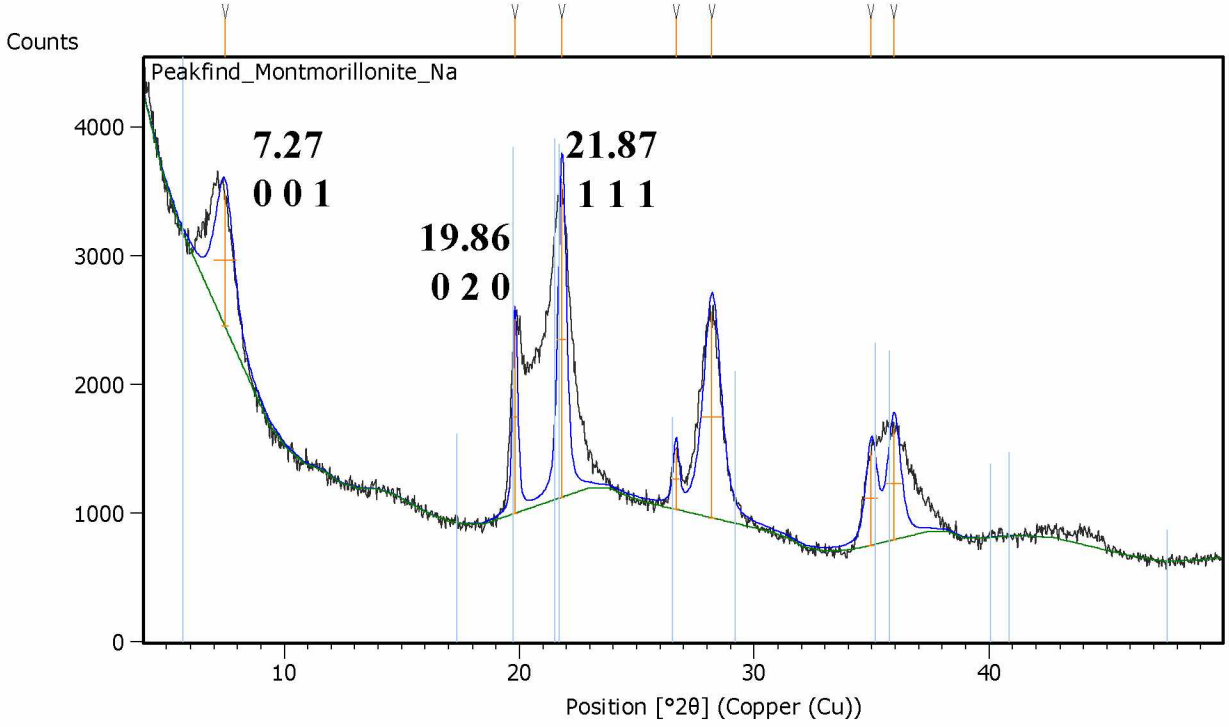

Figure 4.11. Absolute (ω and 2θ) scan results for the Na^{+}-treated montmorillonite pellet sample.

clear donut shape in the pole figure grid (Figures 4.7 and 4.12); conversely, no intensity drop in the pellet absolute scan suggests that no donut shape will be observed in the pole figure results. Strong intensity can be observed as a belt of χ values between 11° and 21°, with empty signals at smaller or larger χ values. A moderate reduction in intensity resulted in a less distinct donut shape, as with the untreated and Ca^{2+}-treated samples (Figure 4.13 and Figure 4.14a, respectively). Untreated sample results demonstrated a small intensity at the center point, compared with the empty signal in the K^{+}-treated sample. The Ca^{2+}-treated and Na^{+}- treated samples demonstrated a mixture of a donut-shaped result and a wing-shaped result, as shown in Figures 4.14a and Figure 4.14b, respectively. The Mg^{2+}-treated sample (Figure 4.15) demonstrated a wing-shaped appearance with strong intensity, which may be an artificial phenomenon induced by the fragmentary geometry of the pellet sample.

For the untreated illite-smectite sample, I also observed a decrease in the intensity of the (001) peak in the absolute scan; however, it is difficult to find a donut shape in the pole figure because it is hard to find a satisfactory peak value for (001) using the HighScore software. After adopting the peak calculated by the software, the pole figure scan did not demonstrate any anomalies. Considering that the K^{+}-treated montmorillonite pole figure results demonstrated a strong donut shape at χ values between 11° and 21°, I assumed that the illite-smectite sample would have similar characteristics. I scanned using a 2θ angle from 5° to 10° (i.e., around 5.717°, which is the (001) peak for montmorillonite), using a fixed χ value at 15° and four ϕ values of 60°, 150°, 240°, and 330°. The results indicated the largest 2θ intensity at 6.858°. Rescans of the pole figure at this 2θ demonstrated a donut shape (Figure 4.16), although scanning at 5.717° did not yield any useful information.

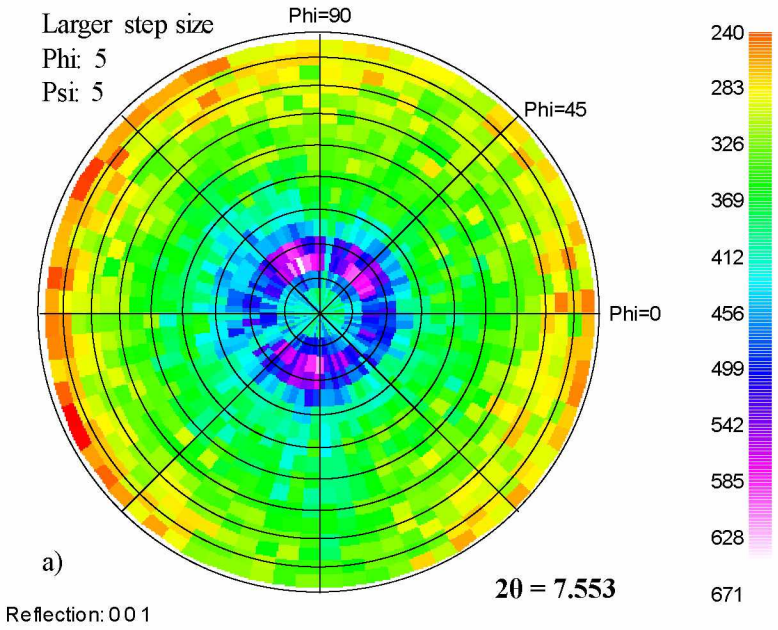

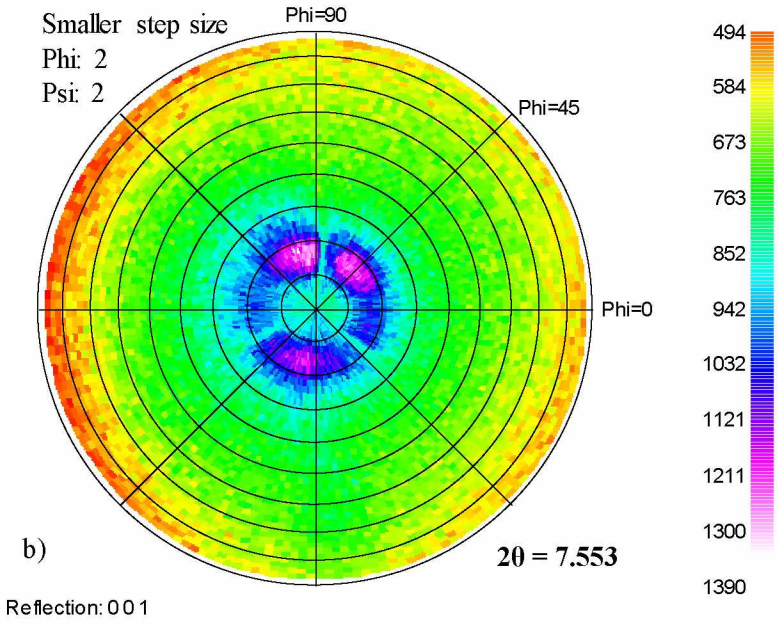

Figure 4.12. Pole figure results for K^+-treated montmorillonite for 2θ of 7.553° for (001) peak: a) larger step size of 5° for φ and 5° for χ; b) finer step size of 2° for φ and 2° for χ with higher resolution.

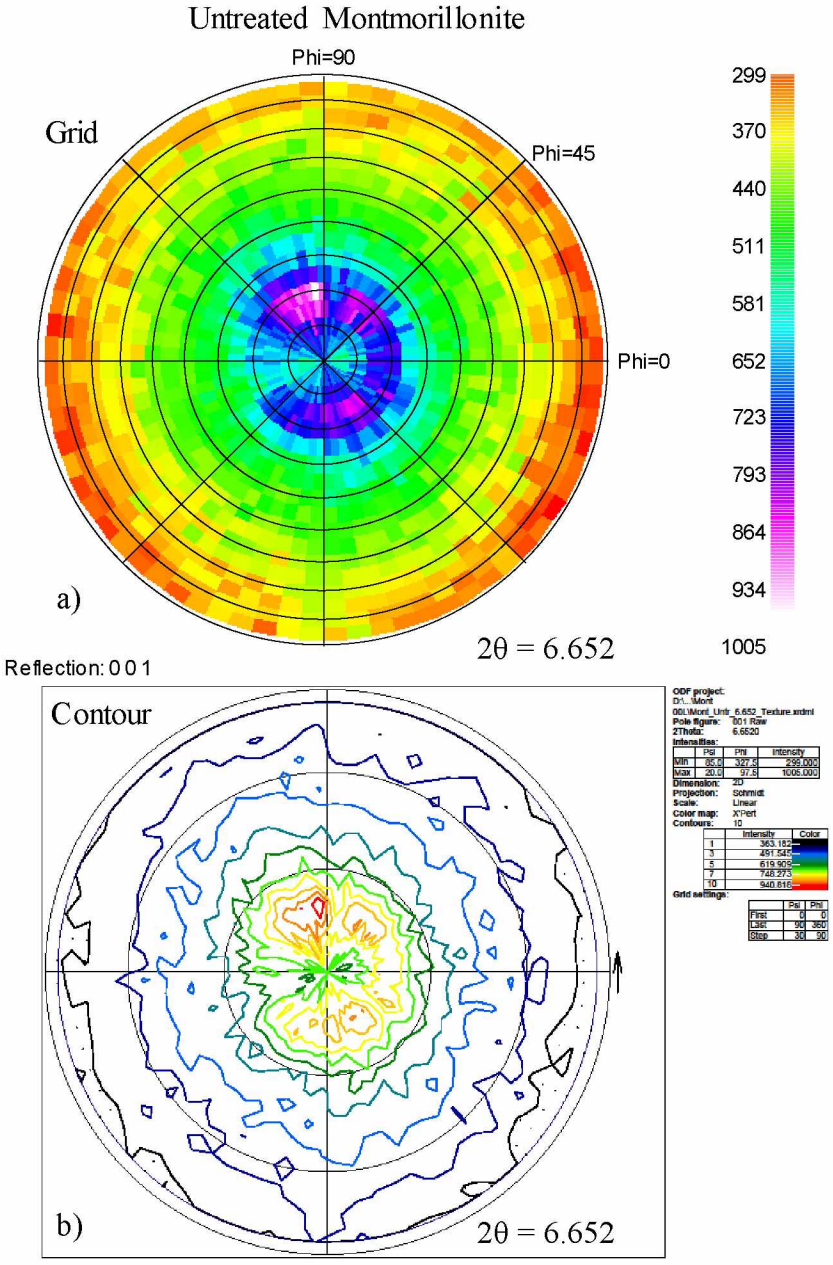

Figure 4.13. Pole figure results for untreated montmorillonite at a 2θ of 6.652° for (001) peak: a) results in a grid plot; b) results in a contour plot.

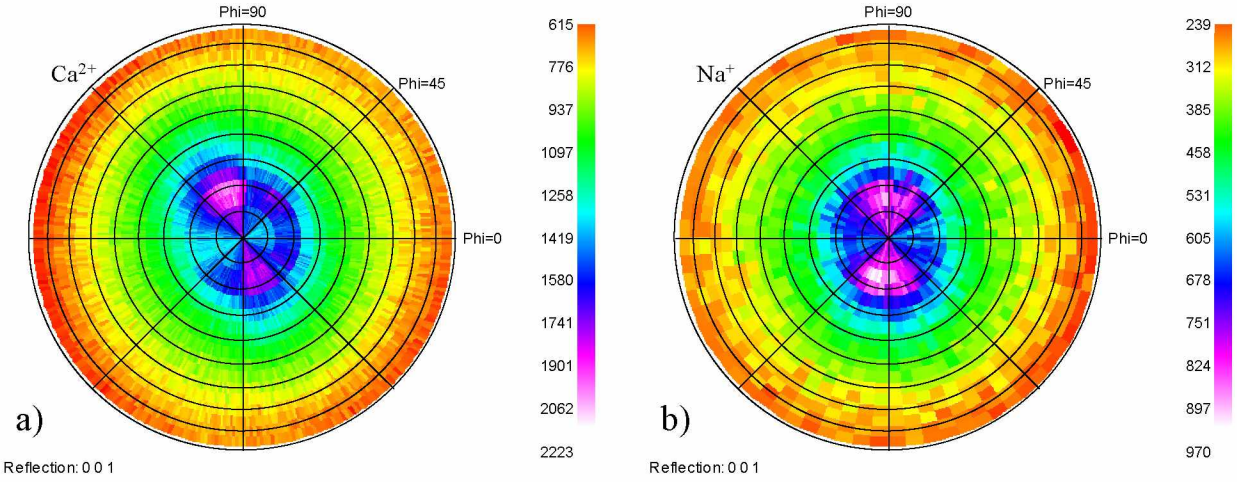

Figure 4.14. Pole figure results for a) Ca^{2+}- and b) Na^{+}-treated montmorillonite for the (001) peak.

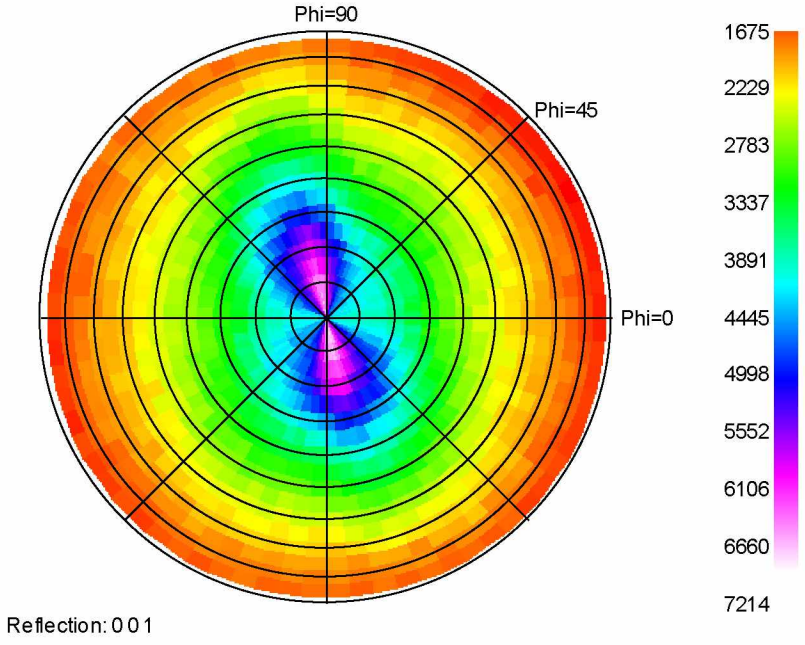

Figure 4.15. Pole figure results for Mg^{2+}-treated montmorillonite for the (001) peak.

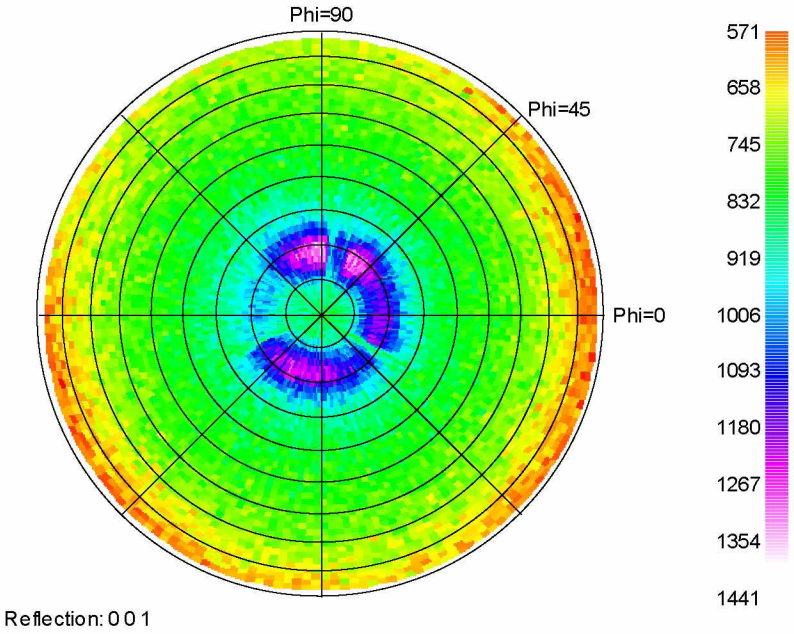

Figure 4.16. Pole figure results for the untreated illite-smectite sample at 2θ of 6.858°.

The strong donut shape in the pole figures also demonstrated low intensity at certain χ values. For example, in the K^+-treated sample, low intensity was measured at χ values of 88°, 220°, and 311° (Figure 4.12a), which is clearer in the results using the smaller step size (Figure 4.12b). For the untreated sample, the results indicated low or near-empty reflections for χ values between 180° and 210°.

The untreated illite-smectite sample also demonstrated a donut-shaped pole figure result (Figure 4.16), similar to the K+-treated montmorillonite. Both samples had strong intensity at χ values between 11° and 21°, with empty signals at smaller or larger χ values. Within the belt of strong intensity area, small areas of low intensity can be found at ϕ values of 88° and 220°, and a large area close to 180°.

Assuming the peaks at (003) and (005) were shifted with the decreased d-spacing that I measured in the absolute scan, and also assuming the clay texture resulted in a peak that could not be matched with the powder test, I measured the pole figure at the inferred 2θ angles, which were calculated using Bragg's law for all the montmorillonite cation treatments. I did not find peaks for any of these 2θ angles.

5. DISCUSSION

5.1 Effects of temperature and cation treatment on the zeta potential

The zeta potential results, especially with the 1mMol solution, demonstrated distinct groupings of divalent and monovalent cations. One interpretation of the results is that a bigger hydrated ionic radius causes a thicker Stern layer, resulting in a thicker diffuse double layer and a lower (more negative) zeta potential. The hydrated radius decreases from Na^+ to K^+, and out of six soils, four of the monovalent cation treatments demonstrated lower zeta potentials for Na^+ compared with K^+ (with the exceptions of chlorite and Copper River). Also, the hydrated radius decreases from Mg^{2+} to Ca^{2+}, and five of the divalent cation treatments demonstrated lower zeta potentials for Mg^{2+} (with the exception of kaolinite). As indicated in the literature, divalent cations compress the diffuse double layer compared with monovalent cations, causing the zeta potential to be higher (less negative) as the concentration of these cations increases. Although not tested here, trivalent cation treatments result in even higher zeta potential values, as demonstrated by Plaza et al. (2014), indicating that higher ionic charges lead to higher zeta potential values.

The electrical potential of the clay particle falls off exponentially with distance, which is described by the Debye-length. Temperature and ionic strength affect the zeta potential by changing the Debye-length. Rytwo (2004) indicated:

$$\lambda_D = \sqrt{\frac{\varepsilon RkT}{2F^2 I}} \qquad \text{(Equation 5.1)}$$

where λ_D is the Debye-length, I is the ionic strength of the electrolyte, ε is the permittivity of free space, R is the dielectric constant, k is the Boltzmann's constant, T is temperature, and F is the elementary charge. In other words, when the ionic strength of a fluid increases, the diffuse

double layer will shrink. Fluids with higher ionic strength, like seawater, cause smaller Debye-lengths in clay particles, leading to higher (less negative) zeta potential values. A common example used to demonstrate the negative correlation of diffuse double layer with ionic strength is that fine-grained particles suspended in a river tend to aggregate and deposit once reaching the saline environment of a delta, because the sea water has higher ionic strength.

Keeping all other variables constant, the cation treatment will affect the Debye-length, and further affect the zeta potential and thus the arrangement of clay particles. A clay dominated by monovalent cations leads to lower zeta potential, and will cause a dispersed structure because of the strong repelling forces, which may limit fluid flow. Conversely, a clay dominated by divalent cations results in a higher zeta potential and weak repelling forces, and the clay particles are more likely to stick together into a flocculated structure. Such a structure has better connectivity among the pore spaces, resulting in higher permeability.

Equation 5.1 also indicates that temperature has a positive correlation with the Debye-length. As the temperature decreases, the Debye-length decreases, resulting in a higher zeta potential. In my results, the negative correlation between zeta potential and temperature is consistent for all samples and cation treatments, and within acceptable experimental error limits. The experimental results indicate that the trend is still valid at subfreezing temperatures. This allows clay particles to flocculate in suspensions at cold temperatures and encourages unfrozen water movement despite higher viscosities. It is not clear, however, whether the higher zeta potential or higher viscosity has more control over the system. The exchangeable cation type also plays a dominant role in the temperature dependence of unfrozen water, with the unfrozen water content in Na^{+}-treated soils being significantly higher than in Ca^{2+}-treated soils at temperatures above -2°C (Kozlowski and Nartowska 2012).

My results indicate that the relationship between temperature and zeta potential is independent of pH. The pH typically varies between 5 and 7 in natural soils; for this range, the tested pH effect on zeta potential fell within 20% for the monovalent cation-treated samples, and within 5% for the divalent cation-treated soils. Based on these results, it is unlikely that the pH is influencing the measured zeta potential; rather, the changes in zeta potential are truly dependent on changes in temperature.

My measurements of zeta potential versus pH are similar to those of other authors. Juang et al. (2002) described a ZPC close to 1 pH in unmodified montmorillonite. Yukselen and Kaya's (2003) measurements of kaolinite in the presence of LiCl, NaCl, $CaCl_2$, and $MgCl_2$ at 10^{-2} and 10^{-4} M concentrations resulted in similar trends, with divalent cations demonstrating higher zeta potential values than monovalent cations. Others reported the ZPC at pH values between 2 and 4 at 20 °C for kaolinite and montmorillonite (Moayedi et al. 2012; Rodríguez and Araujo 2006; Vane and Zang 1997; West and Stewart 1995).

5.2 XRD and texture

One explanation for the XRD results may be how the frozen samples were prepared. For these tests, each sample first was shaped into a cylinder 1.3 cm in diameter and 4-cm long. Next, the sample was dipped into liquid nitrogen and frozen quickly. Although no visible ice lenses were present, I suspect ice lens formation occurred anyway because the upper part of the cylinder that was last to freeze formed a dome shape. Suppose a cylindrical clay specimen is sliced into pieces (Figure 5.1a), with a flat surface cut through the dome structure during the sample preparation. The deformation of the clay from forces during ice formation may lead to the rearrangement of the phyllosilicate sheets. The deformation angle at the cutting surface is large near the vertical cylinder walls and becomes smaller or close to zero at the center of the sample

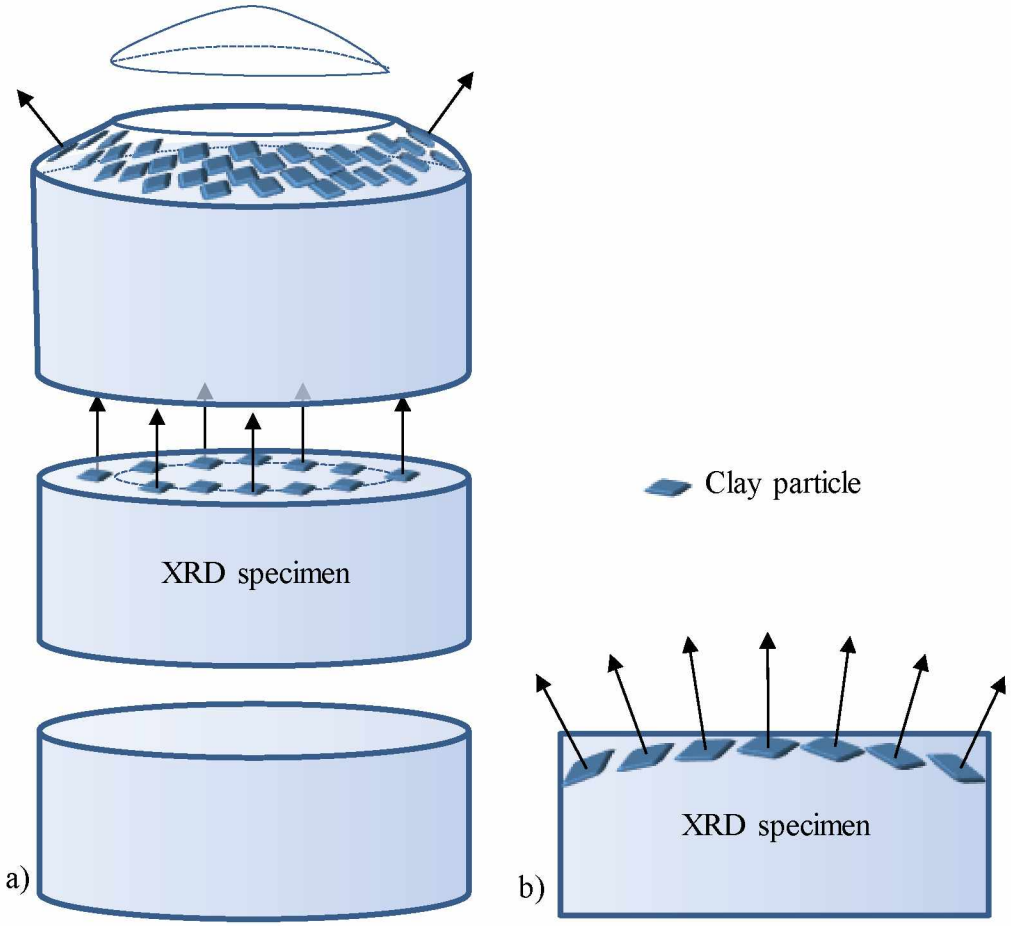

Figure 5.1. Schematic to explain XRD results: a) 3D view of cylindrical soil specimen with dome-shaped top surface; b) 2D view of the XRD specimen, with arrows indicating the clay structure at the cutting surface. Images are not to scale.

(Figure 5.1b). Since the deformation angles will be similar at the same distance from the center of the cylinder, this may lead to a similar donut-shaped orientation. Thus, the rotation of the XRD sample around the center point of the specimen may lead to a donut-shaped pole figure.

Hydration of the montmorillonite samples may happen during preservation or after dehydration with the freeze drying, which can affect the pole figure results. Both freezing the clay samples and freeze-drying them can lead to dehydration of the montmorillonite due to the removal of free water. The loss of water molecules in the interlayers may lead to a decrease in basal spacing. Theoretically, hydration will increase the basal spacing and lead to a decrease of 2θ at the (001) reflection according to Bragg's law; however, all the 2θ results increased at the (001) reflection in the absolute scan for montmorillonite compared to the ICDD standard, suggesting a decreased basal spacing. This suggests that dehydration occurred.

The results for all montmorillonite treatments demonstrated decreased basal spacing and thus dehydration to a certain degree. The untreated and K^+-treated samples displayed a donut-shaped pole figure at the (001) peak. The Ca^{2+}-treated sample demonstrated a mixed or moderate donut-shape, while the Mg^{2+}- and Na^{2+}-treated samples demonstrated wing-like artifacts because of the incomplete pellet size. The donut shape has a strong relationship with the absolute scan results. Only the untreated and K^+-treated montmorillonite samples demonstrated a rapid decrease in intensity of the (001) peak in the pellet sample. This may be due to the preferred alignment of the clay particles. The high intensity diffraction at (001) only occurred when χ was about 15°, making it hard to find this peak in the pellet absolute scan when χ was at 0°. If the intensity is still strong at the (001) peak but shifts to a larger 2θ compared with the ICDD standard, the pole figure will not demonstrate the donut shape. For my samples, this suggests that no similar preferred alignment exists for the untreated and K^+-treated samples.

All the effects noted above need to be examined carefully and eliminated in the redesign of this experiment for future tests. If we can remove all of the sample distortion during preparation, then we can better explore the effects of freezing on the texture of cation-treated clay soils.

6. CONCLUSIONS

To increase our understanding of unfrozen water mass and mobility in frozen soils, this study investigated the temperature effects on the zeta potential and textural changes of cation-treated clay soils. I investigated five homogeneous soils (montmorillonite, kaolinite, illite, illite-smectite, chlorite) and one heterogeneous soil (Copper River soil), each with five different treatments (untreated, and Ca^{2+}, Mg^{2+}, Na^{+}, and K^{+} treatments). I conducted zeta potential measurements at a range of temperatures (-1° to 20°C), and used x-ray diffraction (XRD) to investigate cation effects on clay texture. From the zeta potential and XRD results, the following conclusions can be made:

1. Temperature has a significant effect on the zeta potential of the soil I tested. Most of the samples demonstrated a negative linear trend, with increasing zeta potential at colder temperatures. For the montmorillonite, illite-smectite, and Copper River samples, this linear trend had a steeper slope, while the zeta potential of illite, kaolinite, and chlorite demonstrated a smaller slope and less dependence on temperature. The divalent cation treatments resulted in less negative zeta potentials with temperature changes having less influence, as compared to the monovalent cation treatments. Most significantly, these trends were still valid at the subfreezing temperature (-1°) for nearly all the soils tested.

2. Zeta potential measured in a suspension can be related to soil having a dispersed or flocculated structure. More negative zeta potential (i.e., soil dominated by monovalent cations) will lead to a dispersed structure, whereas less negative zeta potential (i.e., soil dominated by divalent cations) will lead to a flocculated structure.

3. The XRD results of the four homogeneous clay random powder samples (i.e., montmorillonite, kaolinite, illite, and chlorite) matched with the ICCD standards, while the

mixed-layer illite-smectite and heterogeneous Copper River soil were not easily matched with a single standard.

4. The K^+-treated and untreated montmorillonite, and untreated illite-smectite pellet samples demonstrated an apparent decrease of intensity at the (001) peak, and also produced donut-shaped pole figure results. The Na^+- and Mg^{2+}-treated montmorillonite pellet samples demonstrated strong (001) peaks and wing-shaped pole figure results. The Ca^{2+}-treated montmorillonite demonstrated a modest intensity at (001) and a mixture of donut-shaped and wing-shaped pole figure results. The kaolinite, illite, and chlorite pellet results for tested treatments also demonstrated wing-shaped pole figure results, similar to the Mg^{2+}-treated montmorillonite.

5. Unfortunately, the pole figure results may be an artifact of sample preparation rather than reflecting the cation effects on the structure of the clay. More work needs to be done to eliminate these effects during sample preparation.

Improvements could be made to increase the reliability of future testing. For future XRD analysis, it is important to remove any effects from ice lens formation during sample preparation. The frozen clay samples should be taken from the flat end of the frozen cylinder without the dome shape. Alternatively, samples could be placed into a tight cylinder to prevent any volume change upon freezing to eliminate ice lens formation and the doming of the center of the cylindrical sample.

Due to issues with sample preparation, I was unable to conduct XRD analysis for all of the illite-smectite treatments. This soil is more complicated than montmorillonite, as it is a mixed-layer clay. In the zeta potential measurements, both soil types demonstrated similar linear trends with a strong temperature dependence. Since the untreated illite-smectite sample yielded

similar results to montmorillonite, pole figure measurements should be run for all of the illite-smectite treatments and compared with montmorillonite.

Scanning electron microscopy (SEM) should be used to observe the frozen clays, especially montmorillonite, illite-smectite, and the Copper River soil. SEM may not deliver information at the angstrom scale, but if ice in the frozen soil can be removed during freeze drying, and if the voids can be preserved without disturbing the structure of the clay, then SEM may be used to visualize these voids. Scanning at several or tens of nanometers may reveal the internal geometry of these voids and the possible relationship between ice and the clay arrangement, which may increase our understanding of the clay structure at the microaggregate scale.

REFERENCES

Ahlrichs, J. L., and White J. L., 1962. Freezing and lyophilizing alters the structure of bentonite gels. Science: 136(3522), 1116-1118.

Alexander, L., and Klug, H. P., 1948. Basic aspects of X-ray absorption in quantitative diffraction analysis of powder mixtures. Analytical Chemistry: 20(10), 886-889.

Aydin, M., Yano, T., Kilic, S., 2004. Dependence of zeta potential and soil hydraulic conductivity on adsorbed cation and aqueous phase properties. Soil Science Society of America Journal: 68, 450-459.

Barrow, N. J., 1986. Reaction of anions and cations with variable-charge soils. Advances in Agronomy: 38, 183-230.

Bloomfield, V. A., and Dewan, R. K., 1971. Viscosity of liquid mixtures. Journal of Physical Chemistry: 75(20), 3113-3119.

Bolan, N. S., Naidu, R., Syers, J. K., Tillman, R. W., 1999. Surface charge and solute interactions in soils. Advances in Agronomy: 67, 87-140.

Bouyoucos, G., 1917. Classification and measurement of the different forms of water in the soil by means of the dilatometer method. Michigan Agricultural College Experiment Station, Technical Bulletin 36: 939, 713-758.

Bradley, W. F., 1940. The structure scheme of attapulgite. American Mineralogist: 25, 405-410.

Bradley, W. F., Grim, R. E., Clark, G. F., 1937. A study of the behavior of montmorillonite upon wetting. Zeitschrift für Kristallographie: 97, 216-222.

Brindley, W. F., 1961. Chlorite minerals, In Brown, G., (Ed.), The X-ray Identification and Crystal Structure of Clay Minerals: Mineralogical Society, London, UK, pp. 242-296.

Brookhaven, 2010. Instruction Manual for Zetaplus Zeta Potential Analyzer: Brookhaven Instruments, Co., Holtsville, NY, 65 p.

Buatier, M. D., Chauvet, A., Kanitpanyacharoen, W., Wenk, H. R., Ritz, J. F., Jolivet, M., 2012. Origin and behavior of clay minerals in the Bogd fault gouge. Mongolia Journal of Structural Geology: 34, 77-90.

Butt, H., Graf, K., Kappl, M., 2006. Physics and Chemistry of Interfaces: Wiley-VCH Verlag GmbH and Co. KGaA, Weinheim, Germany, 361 p.

Clark, G. L., and Reynolds, D. H., 1936. Quantitative analysis of mine dusts. Industrial and Engineering Chemistry, Analytical Edition: 8(1), 36-40.

Cullity, B. D., and Stock, S. R., 2013. Elements of X-ray Diffraction, third edition: Pearson Education Limited, Harlow, UK, 649 p.

Dąbrowski, A., 2001. Adsorption: from theory to practice. Advances in Colloid and Interface Science: 93(1-3), 135-224.

Debye, P., 1915. Zerstreuung von Röntgenstrahlen. Annalen der Physik: 351, 809-823.

Funck, R. (Ed.), 2008. Glossary of Soil Science Terms 2008: Soil Science Society of America, Madison, WI, 88 p.

Girolami, G. S., 2015. X-Ray Crystallography: University Science Books, Mill Valley, California, 544 p.

Glawdel, T., and Ren, C. L., 2014. Zeta potential measurement. In Li, D., (Ed.), Encyclopedia of Microfluidics and Nanofluidics: Springer, Boston, MA, pp. 3513-3523.

Grim, R. E., 1958. Organization of water on clay mineral surfaces and its implications for the properties of clay-water systems. In Winterkorn H. F., (Ed.), Water and Its Conduction in Soils: Highway Research Board, Washington, D.C., pp. 17-23.

Gruner, J. W., 1934. The structures of vermiculite and their collapse by dehydration. American Mineralogist: 19, 557-575.

Guggenheim, S., and Martin, R. T., 1995. Definition of clay and clay mineral: joint report of the Aipea and CMS nomenclature committees. Clay Minerals: 30(3), 257-259.

Haines, S. H., van der Pluijm, B. A., Ikari, M. J., Saffer, D. M., Marone, C., 2009. Clay fabric intensity in natural and artificial fault gouges: Implications for brittle fault zone processes and sedimentary basin clay fabric evolution. Journal of Geophysical Research: 114, B05406.

Heagler, Jr., J. B., 1964. Clay mineralogy and soil stabilization. Proc., Fifteenth Annual Highway Geology Symposium: Missouri Geological Survey and Water Resources, Rolla, MO, 133-142.

Henniker, J., 1949. The depth of the surface zone of a liquid. Reviews of Modern Physics: 21(2), 322-341.

Hillel, D., 1980. Fundamentals of Soil Physics: Academic Press, San Diego, CA, 413 p.

Howard, B. H., and Lekse, J. W., 2017. Clay Mineralogy. In Romanov, V. (Ed.), Greenhouse Gases and Clay Minerals: Enlightening Down-to-Earth Road Map to Basic Science of Clay-Greenhouse Gas Interfaces: Springer International Publishing AG, Switzerland, pp. 55-65.

Hunter, R. J., 1981. Zeta Potential in Colloid Science: Academic Press, London, UK, 386 p.

Juang, R.-S., Lin, S. Tsao, K., 2002. Mechanism of sorption of phenols from aqueous solutions onto surfactant-modified montmorillonite. Journal of Colloid and Interface Science: 254(2), 234-241.

Kaya, A., and Yukselen, Y., 2005. Zeta potential of clay minerals and quartz contaminated by heavy metals. Canadian Geotechnical Journal: 42, 1280-1289.

Kozlowski, T., and Nartowska, E., 2012. Unfrozen water content in representative bentonites of different origin subjected to cyclic freezing and thawing. Vadose Zone Journal: 12(1), doi:10.2136/vzj2012.0057

Kruse, A. M., Darrow, M. M., Akagawa, S., 2018. Improvements in measuring unfrozen water in frozen soils using pulse nuclear magnetic resonance (P-NMR) method. Journal of Cold Regions Engineering: 32(1), 7 p.

Laird, D. A., 1996. Model for crystalline swelling of 2:1 phyllosilicate. Clays and Clay Minerals: 44(4), 553-559.

Laird, D. A., 2006. Influence of layer charge on swelling of smectites. Applied Clay Science: 34(1-4), 74-87.

Lambe, T. W., 1953. Cold Room Studies, Third Interim Report of Investigations: Arctic Construction and Frost Effects Laboratory, Boston, 19 p.

McEwan, D. M. C., 1961. Montmorillonite minerals. In: Brown, G., (Ed.), The X-ray Identification and Crystal Structures of Clay Minerals: Mineralogical Society, London, UK, 544 p.

Moayedi, H., Huat, B. B. K., Kazemian, S., Mohammad, T. A., 2012. Effect of stabilizer reagents on zeta potential of kaolinite and its relevance to electrokinetic treatment. Journal of Dispersion Science and Technology: 33(1), 103-110.

Morodome, S., and Kawamura, K., 2011. In situ x-ray diffraction study of the swelling of montmorillonite as affected by exchangeable cations and temperature. Clays and Clay Minerals: 59(2), 165-175.

Norrish, K., and Rausell-Colom, J., 1962. Effect of freezing on the swelling of clay minerals. Clay Minerals Bulletin: 5(27), 9-16.

Nersesova, Z. A., and Tsytovich, N. A., 1963. Unfrozen water in frozen soils. Proc., Permafrost International Conference: National Academy of Sciences-National Research Council, Lafayette, IN, 230-234.

Nowakowska, J., 1939. The Refractive Indices of Ethyl Alcohol and Water Mixtures: Loyola University of Chicago, Chicago, IL, 52 p.

Plaza, I., Ontiveros-Ortega, A., Calero, J., Aranda, V., 2014. Implication of zeta potential and surface free energy in the description of agricultural soil quality: effect of different cations and humic acids on degraded soils. Soil and Tillage Research: 146, 148-158.

Rengasamy, P., and Sumner, M. E., 1998. Processes involved in sodic behavior. In Sumner, M. E., and Naidu, R., (Eds.), Sodic Soils: Distribution, Properties, Management, and Environmental Consequences: Oxford University Press, Oxford, UK, pp. 35-50.

Rodríguez, K., and Araujo, M., 2006. Temperature and pressure effects on zeta potential values of reservoir minerals. Journal of Colloid and Interface Science: 300(2), 788-794.

Ross, C. S., and Kerr, P. F., 1931. The clay minerals and their identity. Journal of Sedimentary Research: 1(1), 55-65.

Rytwo, G., 2004. A worksheet model for adsorption/desorption of ions on clay surfaces. In: Wypych F., and Satyanarayana, K. G., (Eds.), Clay Surfaces: Fundamentals and Applications: Elsevier, Ltd, London, UK, pp. 153-183.

Schulthess, C. P., and Sparks, D. L., 1988. A critical assessment of surface adsorption models. Soil Science Society of America Journal: 52(1), 92-97.

Simmonds, C., 1919. Alcohol: Its Production, Properties, Chemistry, and Industrial Applications: Macmillan and Co., London, UK, 574 p.

Suarez, D. L., Roades, J. D., Lavado, R., Grieve, C. M., 1984. Effect of pH on saturated hydraulic conductivity and soil dispersion. Soil Science Society of America Journal: 48, 50-55.

Sposito, G., Skipper, N. T., Sutton, R., Park, S., Soper, A. K., Greathouse, J. A., 1999. Surface geochemistry of the clay minerals. Proceedings of the National Academy of Sciences of the United States of America: 96(7), 3358-3364.

Svensson, P. D., and Hasen, S., 2010. Freezing and thawing of montmorillonite - a time-resolved synchrotron X-ray. Applied Clay Science: 49, 127-134.

Teppen, B. J., 2000. Structural elements of clay minerals, lecture outline for Clay Mineralogy. Retrieved from https://msu.edu/course/css/825/snapshot.afs/teppen/Basic_structural_elements.htm. Accessed: July 12, 2018.

Vane, L. M., and Zang, G. M., 1997. Effect of aqueous phase properties on clay particle zeta potential and electro-osmotic permeability: implications for electro-kinetic soil remediation processes. Journal of Hazardous Materials: 55(1-3), 1-22.

Varadwaj, G. B. B., and Kulamani, P., 2013. Montmorillonite supported metal nanoparticles: an update on syntheses and applications. RSC Advances: 3, 13,583-13,593.

Velde, B. B., 1995. Composition and mineralogy of clay minerals. In Velde, B. B. (Ed.), Origin and Mineralogy of Clays: Clays and the Environment: Springer, Berlin, Germany, pp. 10-19.

Vogel, N., 2012. Surface Patterning with Colloidal Monolayers: Springer, Berlin, Germany, 235 p.

Weirong, J., and Lempe, D. A., 2006. Calculation of viscosities of liquid mixtures using Eyring's theory in combination with cubic equations of state. Chinese Journal of Chemical Engineering: 14(6), 770-779.

West, L. J., and Stewart D. I., 1995. Effect of zeta potential on soil electrokinesis. In Acar, Y. B., and Daniel, D. E. (Eds.), Geoenvironment 2000: Characterization, Containment, Remediation, and Performance in Environmental Geotechnics, Geotechnical Special Publication (GSP) 46: American Society of Civil Engineers, New York, NY, pp. 1535-1549.

Wyman, J., 1931. The dielectric constant of mixtures of ethyl alcohol and water from -5 to 40°. Journal of the American Chemical Society: 53(9), 3,292-3,301.

Yukselen, Y., and Kaya, A., 2003. Zeta potential of kaolinite in the presence of alkali, alkaline earth and hydrolyzable metal ions. Water, Air, and Soil Pollution: 145(1-4), 155-168.